A&A 554, A142 (2013)
DOI: 10.1051/0004-6361/201218974

Astronomy & Astrophysics

H_2O vapor excitation in dusty AGB envelopes

A PACS view of OH 127.8+0.0⋆,⋆⋆

R. Lombaert[1], L. Decin[1,2], A. de Koter[1,2,3], J. A. D. L. Blommaert[1,4], P. Royer[1], E. De Beck[1,5], B. L. de Vries[1], T. Khouri[2], and M. Min[2,3]

[1] Instituut voor Sterrenkunde, KU Leuven, Celestijnenlaan 200D 2401, 3001 Leuven, Belgium
e-mail: robinl@ster.kuleuven.be
[2] Astronomical Institute "Anton Pannekoek", University of Amsterdam, PO Box 94249, 1090 GE Amsterdam, The Netherlands
[3] Astronomical Institute Utrecht, University Utrecht, PO Box 80000, 3508 TA Utrecht, The Netherlands
[4] Department of Physics and Astrophysics, Vrije Universiteit Brussel, Pleinlaan 2, 1050 Brussels, Belgium
[5] Max Planck Institut für Radioastronomie, Auf dem Hügel 69, 53121 Bonn, Germany

Received 7 February 2012 / Accepted 10 April 2013

ABSTRACT

Context. AGB stars lose a large percentage of their mass in a dust-driven wind. This creates a circumstellar envelope, which can be studied through thermal dust emission and molecular emission lines. In the case of high mass-loss rates, this study is complicated by the high optical depths and the intricate coupling between gas and dust radiative transfer characteristics. An important aspect of the physics of gas-dust interactions is the strong influence of dust on the excitation of several molecules, including H_2O.
Aims. The dust and gas content of the envelope surrounding the high mass-loss rate OH/IR star OH 127.8+0.0, as traced by *Herschel* observations, is studied, with a focus on the H_2O content and the dust-to-gas ratio. We report detecting a large number of H_2O vapor emission lines up to $J = 9$ in the *Herschel* data, for which we present the measured line strengths.
Methods. The treatments of both gas and dust species are combined using two numerical radiative transfer codes. The method is illustrated for both low and high mass-loss-rate sources. Specifically, we discuss different ways of assessing the dust-to-gas ratio: 1) from the dust thermal emission spectrum and the CO molecular gas line strengths; 2) from the momentum transfer from dust to gas and the measured gas terminal velocity; and 3) from the determination of the required amount of dust to reproduce H_2O lines for a given H_2O vapor abundance. These three diagnostics probe different zones of the outflow, for the first time allowing an investigation of a possible radial dependence of the dust-to-gas ratio.
Results. We modeled the infrared continuum and the CO and H_2O emission lines in OH 127.8+0.0 simultaneously. We find a dust-mass-loss rate of $(0.5 \pm 0.1) \times 10^{-6}$ $M_\odot$ yr^{-1} and an H_2O ice fraction of 16% ± 2% with a crystalline-to-amorphous ratio of 0.8 ± 0.2. The gas temperature structure is modeled with a power law, leading to a constant gas-mass-loss rate between 2×10^{-5} $M_\odot$ yr^{-1} and 1×10^{-4} $M_\odot$ yr^{-1}, depending on the temperature profile. In addition, a change in mass-loss rate is needed to explain the $J = 1{-}0$ and $J = 2{-}1$ CO lines formed in the outer wind, where the older mass-loss rate is estimated to be 1×10^{-7} $M_\odot$ yr^{-1}. The dust-to-gas ratio found with method 1) is 0.01, accurate to within a factor of three; method 2) yields a lower limit of 0.0005; and method 3) results in an upper limit of 0.005. The H_2O ice fraction leads to a minimum required H_2O vapor abundance with respect to H_2 of $(1.7 \pm 0.2) \times 10^{-4}$. Finally, we report detecting 1612 MHz OH maser pumping channels in the far-infrared at 79.1, 98.7, and 162.9 μm.
Conclusions. Abundance predictions for a stellar atmosphere in local thermodynamic equilibrium yield a twice higher H_2O vapor abundance ($\sim 3 \times 10^{-4}$), suggesting a 50% freeze-out. This is considerably higher than current freeze-out predictions. Regarding the dust-to-gas ratio, methods 2) and 3) probe a deeper part of the envelope, while method 1) is sensitive to the outermost regions. The latter diagnostic yields a significantly higher dust-to-gas ratio than do the two other probes. We offer several potential explanations for this behavior: a clumpy outflow, a variable mass loss, or a continued dust growth.

Key words. circumstellar matter – line: formation – molecular processes – radiative transfer – stars: AGB and post-AGB – stars: mass-loss

1. Introduction

Stars ascending the asymptotic giant branch (AGB) are cool and luminous, and they show pulsations with large periods and amplitudes. Their low effective temperature allows molecules and dust particles to form, with the dust playing an important role in driving the stellar wind these stars exhibit (Kwok 1975). As such, AGB stars are important galactic factories of interstellar gas and dust, contributing significantly to the interstellar mass budget (Whittet 1992; Tielens 2005). More than 70 molecular species have thus far been detected in AGB stars (Olofsson 2008). Of these, carbon monoxide (CO) is one of the most abundant circumstellar molecules after molecular hydrogen (H_2), locking up either all carbon atoms or all oxygen atoms, whichever is the least abundant. When carbon is more abundant (i.e. the carbon-to-oxygen number abundance ratio $n_C/n_O > 1$; defining C-type stars), the molecules and dust species will typically be carbon-based. When oxygen is more abundant (i.e. $n_C/n_O < 1$; M-type), the circumstellar envelope (CSE) will consist mainly of oxygen-based molecules and dust species (Russell 1934; Gilman 1969; Beck et al. 1992).

⋆ *Herschel* is an ESA space observatory with science instruments provided by European-led Principal Investigator consortia and with important participation from NASA.
⋆⋆ Appendix A is available in electronic form at http://www.aanda.org

As the star ascends the AGB, the mass loss increases gradually, eventually leading to the final phase, which is suggested to be a superwind (Renzini 1981). If the AGB star has not yet transitioned into a C-type star when it reaches the superwind phase, it is generally known as an OH/IR star, a name that stems from the presence of strong hydroxyl (OH) masers and infrared (IR) dust emission. For OH/IR stars, the comparison of mass-loss rates determined from the emission of low-excitation CO rotational transitions and those determined from the IR continuum emission appear to indicate surprisingly high dust-to-gas ratios >0.01 (Heske et al. 1990; Justtanont & Tielens 1992; Delfosse et al. 1997). As IR dust emission originates in regions closer to the stellar surface than low-excitation CO emission, therefore tracing a more recent history of the mass-loss behavior, these high dust-to-gas ratios may be spurious and in reality be a manifestation of the recent onset of a superwind (Justtanont & Tielens 1992; Delfosse et al. 1997).

Water (H_2O) vapor has been detected in CSEs of all chemical types, albeit with significantly higher abundances with respect to H_2 in M-type AGB stars ($n_{H_2O}/n_{H_2} \sim 10^{-4}$; Cherchneff 2006; Maercker et al. 2008; Decin et al. 2010b). In these stars, H_2O vapor plays an important role in the energy balance because it is one of the dominant coolants in the innermost regions of the envelope thanks to its large number of far-IR transitions (Truong-Bach et al. 1999). It is, however, difficult to determine H_2O vapor abundances accurately from H_2O vapor emission, owing to, e.g., a complex ro-vibrational molecular structure, multiple excitation mechanisms, and saturation effects (Maercker et al. 2008, 2009; Decin et al. 2010b).

Hitherto, a lack of H_2O observations has been hampering a detailed analysis of the H_2O excitation and abundance. Some H_2O masers and vibrationally excited H_2O lines have been detected from the ground (Menten & Melnick 1989; Menten et al. 2006; see Maercker et al. 2008 for a summary). A detailed survey of multiple H_2O vapor emission lines, however, requires observations made from space. Until recently, only a few space missions have detected circumstellar H_2O emission in the far-IR. The Infrared Space Observatory (ISO, Kessler et al. 1996) found a rich H_2O spectrum for multiple objects, though the spectral resolution was too low to detect anything but the strongest emission lines (Truong-Bach et al. 1999; Barlow et al. 1996; Neufeld et al. 1996).

The recently launched *Herschel* Space Observatory (Pilbratt et al. 2010), allows for a breakthrough in the study of H_2O in AGB sources. OH 127.8+0.0 is the first high mass-loss OH/IR star observed with the Photodetecting Array Camera and Spectrometer (PACS, Poglitsch et al. 2010) onboard *Herschel*. High-J CO emission has also been detected in observations made by the Heterodyne Instrument for the Far-Infrared (HIFI, de Graauw et al. 2010). We aim for a comprehensive study of the physics of H_2O in OH 127.8+0.0 by introducing a combined modeling of the gaseous and the solid state components of the outflow. We determine the gas-mass-loss rate, the radial abundance profile of H_2O vapor, the location of H_2O-ice formation, and the H_2O-ice characteristics, i.e. the ratio of amorphous to crystalline ice particles. We also address the dust-to-gas ratio using three different diagnostics. The first uses the thermal IR continuum of the dust, the second establishes the amount of dust needed to accelerate the outflow to the observed terminal gas velocity, and the third is based on the impact of dust emission on the strength of H_2O lines for a given H_2O vapor abundance. These three diagnostics probe different zones of the circumstellar envelope, for the first time allowing an investigation of a possible radial dependence of the dust-to-gas ratio.

Table 1. Overview of some stellar and circumstellar parameters of OH 127.8+0.0.

Input parameters			
$d_\star$	2.1 kpc	P	1573 days
$L_\star$	$1.0 \times 10^4\ L_\odot$	v_{LSR}	–55.0 km s^{-1}
n_{CO}/n_{H_2}	2.0×10^{-4}	$v_{\infty,g}$	12.5 km s^{-1}
v_{stoch}	1.5 km s^{-1}		

Notes. The distance to the star is denoted as $d_\star$, the stellar luminosity as $L_\star$, the CO abundance as n_{CO}/n_{H_2}, the pulsational period as P, the stellar velocity with respect to the local standard of rest as v_{Lsr}, the stochastic velocity in the outflow as v_{stoch}, and the gas terminal velocity as $v_{\infty,g}$.

2. Target selection and data reduction

2.1. The OH/IR star OH 127.8+0.0

OH 127.8+0.0, also known as V669 Cas, is a high mass-loss-rate AGB star with a relatively simple geometry. VLA maser maps of this object show an almost spherical structure (Bowers & Johnston 1990). The maps hint at possible clumpiness in the gaseous component of the CSE. Estimates for the distance to this source vary from 1.8 kpc to 7 kpc, corresponding to a luminosity range from $6 \times 10^3\ L_\odot$ to $2.6 \times 10^5\ L_\odot$ (Herman & Habing 1985; Engels et al. 1986; Bowers & Johnston 1990; Heske et al. 1990; van Langevelde et al. 1990; Kemper et al. 2002). We follow Suh & Kim (2002), who take the pulsational phase into account while modeling the spectral energy distribution (SED). They find a luminosity of $L_{\star,max} = 3.6 \times 10^4\ L_\odot$ at light maximum, $L_{\star,min} = 1.0 \times 10^4\ L_\odot$ at light minimum, and an average luminosity of $L_{\star,avg} = 2.7 \times 10^4\ L_\odot$. The last agrees with the period-luminosity relations derived by Whitelock et al. (1991), taking the pulsational period equal to $P = 1537 \pm 17.7$ days (Suh & Kim 2002). Since the IR ISO Short Wavelength Spectrometer (SWS; de Graauw et al. 1996) data (observed in January 1998), as well as the PACS data (January 2010) were taken at light minimum, we take $L_\star = 1.0 \times 10^4\ L_\odot$. This value corresponds to a distance of $d_\star = 2.1$ kpc. We assume a CO abundance of $n_{CO}/n_{H_2} = 2.0 \times 10^{-4}$ (Decin et al. 2010a). The gas terminal velocity $v_{\infty,g} = 12.5$ km s^{-1} is determined well by the width of the low-excitation transitions of CO (see Fig. 1), and is used as the primary constraint on the gas velocity field. The velocity of the system with respect to the local standard of rest is $v_{LSR} = -55.0$ km s^{-1} (De Beck et al. 2010). The stochastic velocity of the gas in the wind is taken to be $v_{stoch} = 1.5$ km s^{-1} (Skinner et al. 1999). The stellar and circumstellar parameters for OH 127.8+0.0 are summarized in Table 1.

The CSE has been modeled by several authors who report high gas-mass-loss rates of $\dot{M}_g \sim 10^{-5}$–$10^{-4}\ M_\odot$ yr^{-1} (Netzer & Knapp 1987; Bowers & Johnston 1990; Justtanont & Tielens 1992; Loup et al. 1993; Suh & Kim 2002; De Beck et al. 2010). Owing to the high mass-loss rate, the density in the CSE is high enough for H_2O ice to freeze out, shown by a strong absorption band around 3.1 μm (Omont et al. 1990; Justtanont & Tielens 1992; Sylvester et al. 1999).

2.2. Observations and data reduction

2.2.1. PACS

We combined three PACS observations of OH 127.8+0.0 with six *Herschel* observation identifiers (obsids, 1342189956 up

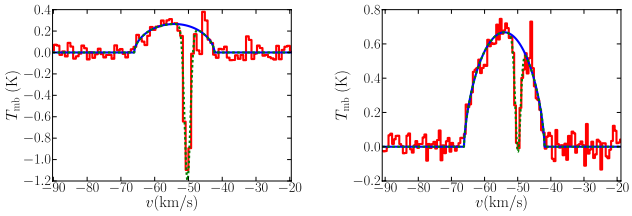

Fig. 1. Ground-based JCMT observations of OH 127.8+0.0. *The left panel* shows the CO $J = 2-1$ observation in red, whereas the CO $J = 3-2$ is shown in the right panel. The dashed green curve gives a line profile fit including a soft-parabola and a Gaussian function. The full blue curve indicates only the soft-parabola component, which represents the emission coming from the CSE of OH 127.8+0.0. The Gaussian component reproduces the interstellar absorption.

to 1342189961) taken in January 2010. The first observation was performed with the standard Astronomical Observing Template (AOT) for SED. The two others were originally obtained as part of the AOT fine-tuning campaign. The corresponding observing modes are identical to the standard one, except that alternative chopping patterns were used. All observations were reduced with the appropriate interactive pipeline in HIPE 8.0.1, with calibration set 32. The absolute flux calibration is based on the calibration block (i.e. the initial part of the observation, performed on internal calibration sources) and is accurate to about 20%. We have rebinned the data with an oversampling factor of 2, i.e. a Nyquist sampling with respect to the native instrumental resolution. Consistency checks between the pipeline products of the observations made with the three chopping patterns show excellent agreement, well within the calibration uncertainty. Since OH 127.8+0.0 is a point source, the spectrum is extracted from the central spaxel and then point-source-corrected in all bands. We list the integrated line strengths of detected emission lines in Table A.1. The line strengths were measured by fitting a Gaussian on top of a continuum to the lines. The reported uncertainties include the fitting uncertainty and the absolute flux calibration uncertainty of 20%. Measured line strengths are flagged as line blends if they fulfill at least one of two criteria: 1) the full width at half maximum (FWHM) of the fitted Gaussian is larger than the FWHM of the PACS spectral resolution by at least 30%; 2) multiple H_2O transitions have a central wavelength within the FWHM of the fitted central wavelength of the emission line. Other molecules are not taken into account. We caution the reader that the reported line strengths not flagged as line blends may still be affected by emission from other molecules or H_2O transitions not included in our modeling.

2.2.2. HIFI

OH 127.8+0.0 was observed with the HIFI instrument in the HIFI Single Point AOT with dual-beam switching. The observed rotationally excited lines in the vibrational groundstate include the $J = 5-4$ (obsid 1342201529, observed in July 2010) and $J = 9-8$ (obsid 1342213357, observed in January 2011) transitions. These observations were made in the framework of the SUCCESS *Herschel* guaranteed time program (Teyssier et al., in prep.). The data were retrieved from the *Herschel* Science Archive[1] and reduced with the standard pipeline for HIFI observations in HIPE 8.1. The level 2 pipeline products were then reduced further by first applying baseline subtraction, followed by the conversion to main-beam temperature with main-beam efficiencies taken from the HIFI observers' manual (version 2.4, Sect. 5.5.2.4), and finally by taking the mean of vertical and horizontal polarizations. Finally, the $J = 5-4$ line was rebinned to a resolution of 1.3 km s^{-1} and the $J = 9-8$ line to a resolution of 2.2 km s^{-1}. The absolute flux calibration uncertainty of HIFI is estimated to be ∼10% according to the HIFI Observers' Manual (version 2.4, Sect. 5.7). However, owing to the low signal-to-noise of ∼4–5 in the observed lines, we adopt a more conservative calibration uncertainty of 20%.

[1] http://herschel.esac.esa.int/Science_Archive.shtml

2.2.3. Ground-based data

Data for several rotationally excited lines of CO in the vibrational groundstate were obtained with the ground-based *James Clerk Maxwell* Telescope (JCMT) and the ground-based 30 m telescope operated by the Institut de Radioastronomie Millimétrique (IRAM). The JCMT observations include the $J = 2-1$ (observed in September 2002), $J = 3-2$ (July 2000), $J = 4-3$ (April 2000) and $J = 6-5$ (November 2002) transitions. The first three JCMT transitions were published by Kemper et al. (2003), and the $J = 6-5$ transition was presented by De Beck et al. (2010). Heske et al. (1990) published the IRAM observations including the $J = 1-0$ (June 1987) and $J = 2-1$ (February 1988) transitions. We refer to these publications for the technical details concerning the data reduction. In this study, the $J = 4-3$ transition is not taken into account. Considering that the line formation regions of the $J = 3-2$ and the $J = 4-3$ lines largely overlap, one can expect consistent line-integrated fluxes for the two lines when observed with the same telescope. No emission in the $J = 4-3$ observation is significantly detected, while a line-integrated flux well above the 3σ noise level of the JCMT observation is estimated from the $J = 3-2$, as well as from the other observations. This discrepancy can be caused by certain model assumptions; e.g., we do not consider that the CO $J = 4$ level may be depopulated by pumping via a molecule other than CO and therefore result in a significantly decreased expected $J = 4-3$ emission or by an observational issue, e.g., suboptimal pointing of the telescope. The cause of the discrepancy is not clear, so that it is safer to exclude the observation from the study.

Strong CO emission at the JCMT off-source reference position contaminates the on-source $J = 2-1$ and $J = 3-2$ JCMT observations after background subtraction. As shown in Fig. 1, the lines can be fitted with an analytical function equal to the sum of a soft-parabola function representing the emission profile (following De Beck et al. 2010) and a Gaussian function for the negative flux contribution. The Gaussian component in the fit to both observations is centered on ∼50 km s^{-1} and has a width of ∼1 km s^{-1}, which is a typical value for the turbulent velocity in the interstellar medium (Redfield & Linsky 2008), assuming the CO emission in the off-source observation has an interstellar origin. For the CO $J = 2-1$ and $3-2$ JCMT observations, we use an absolute flux calibration uncertainty of 30% (Kemper et al. 2003). The CO $J = 6-5$ has a low signal-to-noise ratio and is therefore treated as an upper limit with an absolute flux calibration uncertainty of 40%. From the soft-parabola component of the $J = 3-2$ observation, which both has a high signal-to-noise and suffers less from the off-source contamination than the $J = 2-1$ line, we derive a gas terminal velocity $v_{\infty,g} \sim 12.5$ km s^{-1}. For the IRAM observations, we use the line profiles published by Heske et al. (1990), who performed a careful background subtraction to avoid an off-source CO contribution. We assume an absolute flux calibration uncertainty of

20% for the IRAM data, taking the uncertainty involved with the background subtraction into account (Heske et al. 1990).

2.2.4. Spectral energy distribution

The SED (see Sect. 4.1) is constructed from data obtained by the ISO-SWS and Long Wavelength Spectrometer (LWS; Clegg et al. 1996; Swinyard et al. 1996) instruments, as well as from PACS data. The ISO-SWS data were retrieved from the Sloan et al. (2003) database. The ISO-LWS data were taken from the ISO Data Archive[2] and rescaled to the calibrated ISO-SWS data. The ISO-LWS data are not background-subtracted, whereas the PACS data are, suggesting that more flux at long wavelengths is expected in the ISO-LWS data owing to OH 127.8+0.0's location in the galactic plane. In addition, the PACS photometric data at 70 μm and 160 μm (not shown here) coincide with the PACS spectrum. The uncertainty on the absolute flux calibration of the PACS photometric data is below 15% (Groenewegen et al. 2011). Taking these considerations into account, the ISO and PACS data agree well. The ISO-SWS and PACS data were all taken at the light minimum pulsational phase, so we assume the same stellar luminosity for both data sets and refer to the work of Suh & Kim (2002) for pulsationally dependent IR continuum modeling including photometric data. Because OH 127.8+0.0 lies in the galactic plane, we corrected for interstellar reddening following the extinction law of Chiar & Tielens (2006), with an extinction correction factor in the K-band of $A_K = 0.24$ mag (Arenou et al. 1992).

3. Methodology

To get a full, consistent understanding of the entire CSE, information from both gas and dust diagnostics should be coupled. Kinematical, thermodynamical, and chemical information about the circumstellar shell is derived from the molecular emission lines and the dust features by making use of two radiative transfer codes. The non-local thermodynamic equilibrium (NLTE) line radiative transfer code GASTRoNOoM (Decin et al. 2006, 2010a) calculates the velocity, temperature, and density profiles of the gas envelope, the level populations of the individual molecules, and the line profiles for the different transitions of each molecule. The continuum radiative transfer code MCMax (Min et al. 2009) calculates the dust temperature structure and the IR continuum of the envelope. These numerical codes are briefly described in Sects. 3.1 and 3.2. In Sects. 3.3 to 3.5, we describe how the two codes are combined with an emphasis on the physical connections between the gaseous and dusty components. We end this section by discussing the advantage of our approach in light of molecular excitation mechanisms.

3.1. Line radiative transfer with GASTRoNOoM

3.1.1. The kinematical and thermodynamical structure

The kinematical and thermodynamical structure of the CSE is calculated by solving the equations of motion of gas and dust and the energy balance simultaneously (Decin et al. 2006). We assume a spherically symmetric gas density distribution. The radial gas velocity profile $v_g(r)$ depends on the momentum transfer via collisions between gas particles and dust grains, the latter being exposed to radiation pressure from the central star. This momentum coupling is assumed to be complete (Kwok 1975), such that the radiative force on the dust grains can be equated to the gas drag force. The population of dust grains has the assumed size distribution

$$n_d(a, r)\,\mathrm{d}a = A(r)\,a^{-3.5}\,n_H(r)\,\mathrm{d}a, \quad (1)$$

where n_H is the total hydrogen number density, a the radius of the spherical dust grain, and $A(r)$ an abundance scale factor giving the number of dust particles with respect to hydrogen (Mathis et al. 1977). The minimum grain size considered is $a_{min} = 0.005$ μm and the maximum grain size $a_{max} = 0.25$ μm. Höfner (2008) suggests that large grains are needed in an M-type AGB CSE to be able to drive the stellar wind through photon scattering. Norris et al. (2012) have detected these large grains, with sizes up to $a \sim 0.3$ μm, backing up our assumption of a maximum grain size of ~0.25 μm.

The gas kinetic temperature profile $T_g(r)$ depends on the heating and cooling sources in the CSE. The heating sources taken into account are gas-grain collisional heating, photoelectric heating from dust grains, heating by cosmic rays, and heat exchange between dust and gas. The cooling modes include cooling by adiabatic expansion and the emission from rotationally excited CO and H_2O levels and vibrationally excited H_2 levels. As the difference between dust and gas velocity, the drift velocity $w(a, r)$ directly enters the equation for collisional gas heating. To calculate the contribution from the heat exchange between gas and dust, the dust-temperature profile $T_d(r)$ needs to be known as well. Decin et al. (2006) approximate this profile by a power law of the form

$$T_d(r) = T_\star \left(\frac{R_\star}{2r}\right)^{2/(4+s)}, \quad (2)$$

where $s \approx 1$ (Olofsson in Habing & Olofsson 2003). We address the dust temperature profile further in Sect. 3.5.1.

3.1.2. Radiative transfer and line profiles

The solution of the radiative transfer equations coupled to the rate equations and the calculation of the line profiles are described by Decin et al. (2006). In this work we adopt MARCS theoretical model spectra (Decin & Eriksson 2007; Gustafsson et al. 2008; Decin et al. 2010a) to improve the estimate of the stellar flux, as compared to a blackbody approximation. This results in more realistic absolute intensity predictions for the less abundant molecules with stronger dipole moments like H_2O, which are mainly excited by near-IR radiation from the central star (Knapp & Morris 1985). For an extensive overview of the molecular data used in this study, we refer to the appendix in Decin et al. (2010a).

3.2. Continuum radiative transfer with MCMax

MCMax is a self-consistent radiative transfer code for dusty environments based on a Monte Carlo simulation (Min et al. 2009). It predicts the dust temperature stratification and the emergent IR continuum of the circumstellar envelope. We use a continuous distribution of ellipsoids (CDE, Bohren & Huffman 1983; Min et al. 2003) to describe the optical properties of the dust species. A CDE provides mass-extinction coefficients κ_λ – or cross-sections per unit mass – for homogeneous particles with a constant volume, where the grain size a_{CDE} is the radius of a volume-equivalent sphere. The CDE particle-shape model is only valid in the Rayleigh limit, i.e. when $\lambda \gg a_{CDE}$. For photons

[2] http://iso.esac.esa.int/iso/ida/

at wavelengths $\lambda \gg a_{\rm CDE}$, both inside and outside the grain, the mass-absorption coefficients $\kappa^{\rm a}_{\lambda,{\rm CDE}}$ are independent of particle size, and the mass-scattering coefficients $\kappa^{\rm s}_{\lambda,{\rm CDE}}$ are negligible.

MCMax does not include a self-consistent momentum transfer modeling procedure, i.e. the IR continuum is calculated based on a predetermined dust density distribution $\rho_{\rm d}(r)$. As a standard, this density distribution is assumed to be smooth, following the equation of mass conservation $\dot{M}_{\rm d}(r) = 4\pi\, r^2\, v_{\rm d}(r)\, \rho_{\rm d}(r)$, with $\dot{M}_{\rm d}(r) = \dot{M}_{\rm d}$ the dust-mass-loss rate, which is assumed to be constant, and $v_{\rm d}(r)$ the dust velocity profile, which is taken to be constant and equal to the terminal dust velocity $v_{\infty,{\rm d}}$. Because the drift velocity is usually unknown, the dust terminal velocity is often equated to the gas terminal velocity $v_{\infty,{\rm g}}$. In most cases, this simplification is found to be inaccurate, because the drift is nonzero (Kwok 1975). A possible improvement includes a customized density profile that takes a nonzero drift into account, as well as the acceleration of the dust grains derived from momentum transfer modeling (see Sect. 3.4.1). In practice, the optical depth $\tau_\nu = 1$ surface in the IR lies outside the acceleration region for high enough dust densities, so an improved density distribution in this region is not likely to affect the IR continuum of high mass-loss-rate stars. On the other hand, the effect on dust emission features in low mass-loss-rate stars may be significant.

3.3. The five-step modeling approach

We solve the line radiative transfer and continuum radiative transfer using a five-step approach.

1. The dust thermal IR continuum is modeled using MCMax to obtain an initial estimate of the dust composition, dust temperature, and dust-mass-loss rate.
2. The kinematics and thermodynamics of the gas shell are calculated with GASTRoNOoM incorporating dust extinction efficiencies, grain temperatures, and the dust-mass-loss rate from MCMax. This provides a model for the momentum transfer from dust to gas, hence a dust velocity profile.
3. Given a dust-mass-loss rate, the dust velocity profile leads to a new dust-density profile for which the IR continuum model is updated.
4. The gas kinematical and thermodynamical structures are recalculated with the updated dust parameters.
5. Line radiative transfer with GASTRoNOoM is performed and line profiles are calculated.

This five-step approach is repeated by changing various shell parameters such as the mass-loss rate and envelope sizes, until the CO molecular emission data are reproduced with sufficient accuracy. This provides a model for the thermodynamics and the kinematics of the envelope. The CO molecule is an excellent tracer for the thermodynamics of the entire gas shell because it is easily collisionally excited and relatively difficult to photodissociate.

3.4. Incorporating gas diagnostics into the dust modeling

3.4.1. Dust velocity profile

The dust velocity profile $v_{\rm d}(r)$ cannot be derived from the IR continuum emission of the dust. However, the gas terminal velocity is determined well from the width of CO emission lines observed by ground-based telescopes, providing a strong constraint on the gas kinematical model. In conjunction with the drift velocity $w(a, r)$, the gas velocity profile $v_{\rm g}(r)$ leads to $v_{\rm d}(r)$. If the momentum coupling between gas and dust is complete, one can write the drift velocity at radial distance r and for grain size a as (Kwok 1975; Truong-Bach et al. 1991; Decin et al. 2006)

$$
\begin{aligned}
w(a,r) &= v_{\rm K}(a,r)\left[\sqrt{1+x(a,r)^2} - x(a,r)\right]^{1/2}, \text{ with}\\
v_{\rm K}(a,r) &= \sqrt{\frac{v_{\rm g}(r)}{\dot{M}_{\rm g}(r)c}\int Q_\lambda(a) L_\lambda {\rm d}\lambda},\\
x(a,r) &= \frac{1}{2}\left[\frac{v_{\rm T}(r)}{v_{\rm K}(a,r)}\right]^2, \text{ and}\\
v_{\rm T}(r) &= \frac{3}{4}\left[\frac{3kT_{\rm g}(r)}{\mu m_{\rm H}}\right]^{1/2}.
\end{aligned}
$$

Here, $Q_\lambda(a)$ are the dust extinction efficiencies, L_λ is the monochromatic stellar luminosity at wavelength λ, $v_{\rm T}(r)$ the Maxwellian velocity of the gas, $T_{\rm g}(r)$ the gas kinetic temperature, k Boltzmann's constant, μ the mean molecular weight of the gas, and $m_{\rm H}$ the mass of the hydrogen atom.

GASTRoNOoM works with grain-size dependent extinction efficiencies, whereas we use grain-size independent CDE models for the circumstellar extinction in MCMax. As a result, the grain-size dependent drift velocity $w(a, r)$ has to be converted to a grain-size independent average drift velocity $\bar{w}(r)$. For simplicity, we assume that the factor $\left[\sqrt{1+x(r)^2} - x(r)\right]^{1/2}$ has a negligible effect. This assumption holds in the outer region of the CSE, where the drift velocity is much higher than the thermal velocity. The weighted drift velocity $\bar{w}(r)$ with respect to the grain-size distribution $n_{\rm d}(a, r)$ from Eq. (1) can be written as

$$
\bar{w}(r) = \frac{\int v_{\rm K}(a,r)\, n_{\rm d}(a,r)\, {\rm d}a}{\int n_{\rm d}(a)\, {\rm d}a}.
$$

Assuming a grain-size distribution between lower limit $a_{\rm min}$ and upper limit $a_{\rm max}$, this leads to

$$
\bar{w}(r) = \frac{g_{\rm a}\, v_{\rm K}(a_0, r)}{a_0}, \tag{3}
$$

for an arbitrary grain size a_0 of a given drift velocity, with the weighting factor $g_{\rm a} = 1.25\,(a_{\rm max}^{-2} - a_{\rm min}^{-2}) \times (a_{\rm max}^{-2.5} - a_{\rm min}^{-2.5})^{-1}$. For GASTRoNOoM, this yields a weighting factor of $g_{\rm a} \simeq 0.09$. Combining $v_{\rm d}(r) = \bar{w}(r) + v_{\rm g}(r)$ with the equation of mass conservation, we find a density distribution $\rho_{\rm d}(r)$ that can be used in MCMax.

3.5. Incorporating dust diagnostics into the gas modeling

The formation of dust species in the stellar wind has a big influence on the thermal, dynamical, and radiative structure of the envelope; e.g., dust-gas collisions cause heating of the gas and drive the stellar wind, while the thermal radiation field of the dust is an important contributor to the excitation of several molecules, such as H_2O. An accurate description of the dust characteristics is thus paramount in any precise prediction of the molecular emission. Here, we discuss the treatment of the dust temperature, the inner shell radius, dust extinction efficiencies, and the dust-to-gas ratio. The effects of a more consistent coupling between dust and gas characteristics is described in Sect. 3.6.

3.5.1. Dust temperature and the inner shell radius

We include an average dust-temperature profile calculated with MCMax in our gas modeling, instead of the power law in Eq. (2).

This average profile is calculated assuming that the dust species are in thermal contact, i.e. distributing the absorbed radiation among all dust species such that they are at the same temperature at every radial point. We still use the independent dust temperature profiles of the different dust species – rather than the average profile – in the IR continuum modeling.

The pressure-dependent dust-condensation temperature is determined following Kama et al. (2009), setting the inner radius $R_{\rm i,d}$ of the dust shell. Since this inner radius indicates the starting point of momentum transfer from dust to gas in the CSE, it is assumed to be the inner radius $R_{\rm i,g}$ of the GASTRoNOoM model as well.

3.5.2. Dust extinction efficiencies

Decin et al. (2006) assume extinction efficiencies for spherical dust particles with a dust composition typical of OH/IR stars, where the main component is amorphous olivine (Mg_x,Fe_{1-x})$_2SiO_4$ (Justtanont & Tielens 1992). However, if one determines the dust composition independently by modeling the IR continuum, consistent extinction efficiencies can be derived. To convert the grain-size independent CDE mass-extinction coefficients κ_λ used in MCMax to the grain-size dependent extinction efficiencies $Q_\lambda(a)$ used in GASTRoNOoM, the wavelength-dependent extinction coefficient χ_λ is written as

$$\chi_\lambda = n_{\rm d}(a)\,\sigma_\lambda(a) = n_{\rm d}(a)\,Q_\lambda(a)\,\pi\,a^2,$$

where $n_{\rm d}(a)$ is the number density of the dust particles in cm^{-3} (see Eq. (1)) and $\sigma_\lambda(a)$ the extinction cross-section in cm^2. By taking $\kappa_\lambda = \chi_\lambda\,\rho_{\rm d}^{-1}$, with $\rho_{\rm d}$ the mass density of the dust particles, it follows that

$$Q_\lambda(a) = \frac{4}{3}\,\kappa_\lambda\,\rho_{\rm s}\,a,$$

assuming the grains have a homogeneous grain structure. Here, $\rho_{\rm s}$ is the average specific density of a single dust grain. This conversion can be done as long as the Rayleigh assumption required for the CDE particle-shape model is valid for every grain size a used in GASTRoNOoM (see Sect. 3.2).

3.5.3. The dust-to-gas ratio

The dust-to-gas ratio in AGB environments is a rather ambiguous quantity and is typically assumed to be $\psi \sim 0.005$–0.01 (e.g. Whitelock et al. 1994). Different approaches can be used to estimate the dust-to-gas ratio. We assume a constant dust-to-gas ratio throughout the envelope in all of these definitions:

1. Models of high-resolution observations of CO emission constrain the gas-mass-loss rate $\dot{M}_{\rm g}$, hence the radial profile of the gas density $\rho_{\rm g}(r)$ using the equation of mass conservation. The dust-mass-loss rate $\dot{M}_{\rm d}$ is determined from fitting the thermal IR continuum of the dust. We note that the dust velocity field used to convert $\dot{M}_{\rm d}$ into a radial dust-density profile $\rho_{\rm d}(r)$ is obtained from the GASTRoNOoM-modeling and accounts for drift between dust grains and gas particles. The dust-to-gas ratio is then given by
$$\psi_{\rm dens} = \frac{\rho_{\rm d}}{\rho_{\rm g}} = \left(\frac{\dot{M}_{\rm d}}{v_{\infty,{\rm d}}}\right)\left(\frac{v_{\infty,{\rm g}}}{\dot{M}_{\rm g}}\right).$$
2. Given the total mass-loss rate $\dot{M} = \dot{M}_{\rm g} + \dot{M}_{\rm d}$, and the composition and size distribution of the dust species, GASTRoNOoM calculates the amount of dust needed in the envelope to accelerate the wind to its gas terminal velocity $v_{\infty,{\rm g}}$ by solving the momentum equation. This approach depends on the efficiency of the momentum coupling between the dust and gas components of the CSE. We assume complete momentum coupling, but we point out that this assumption does not always hold (MacGregor & Stencel 1992; Decin et al. 2010a). The empirical value of $v_{\infty,{\rm g}}$ is determined from high-resolution observations of low-excitation emission lines, such as CO $J = 1$–0. The dust-to-gas ratio determined via this formalism will be denoted as $\psi_{\rm mom}$.
3. In case of a high mass-loss rate, CO excitation is not sensitive to the dust emission, which allows one to constrain the gas kinetic temperature profile and the $\dot{M}_{\rm g}$-value by modeling the CO emission. In contrast, a main contributor to the excitation of H_2O is thermal dust emission. This allows one to determine the amount of dust required to reproduce the observed line intensities for a given H_2O vapor abundance. This leads to a dust-to-gas ratio denoted as $\psi_{\rm H_2O}$, which depends on the adopted H_2O vapor abundance.

3.6. Advantages of combined dust and gas modeling: molecular excitation

Calculating theoretical line profiles for molecular emission strongly depends on several pumping mechanisms to populate the different excitation levels, some of which are connected to the dust properties of the outflow. The most common mechanisms to populate the rotational levels in the vibrational groundstate include:

1. Collisional excitation: low-energy excitation is usually caused by collisions between a molecule and H_2. This mechanism becomes more important with higher densities due to the more frequent collisions. For instance, the ground-vibrational level of CO is easily rotationally excited (transitions at $\lambda > 200\,\mu$m).
2. Excitation by the near-IR radiation field: The near-IR stellar continuum photons can vibrationally excite molecules. The vibrational de-excitation then happens to rotationally excited levels in lower vibrational states, with the rotational level being determined by quantum-mechanical selection rules. For instance, the first vibrational state ($\lambda \sim 4.2\,\mu$m) of CO and the $\nu_1 = 1$ ($\lambda \sim 2.7\,\mu$m), $\nu_2 = 1$ ($\lambda \sim 6.3\,\mu$m), and $\nu_3 = 1$ ($\lambda \sim 2.7\,\mu$m) vibrational states of H_2O are excited this way. If the dust content of a CSE is high, a significant fraction of the stellar near-IR photons are absorbed and re-emitted at longer wavelengths, and cannot be used for vibrational excitation of molecules.
3. Excitation by the diffuse radiation field: The diffuse field is mainly the result of thermal emission by dust and the interstellar background radiation field. These photons allow rotational excitation to levels that require energies that are too high to be accessed through collisional excitation, and too low to be excited by absorption from the stellar near-IR radiation field. For instance, the ground-vibrational level of H_2O is rotationally excited through photons provided by the diffuse field ($\lambda \sim 10$–$200\,\mu$m). Increasing the dust content causes more pumping through this channel.

The relative importance of these mechanisms strongly depends on the Einstein coefficients and on the local physical conditions of both the dust and gas components of the CSE.

To show the effect of dust on line emission predictions for a few selected lines of CO and H_2O in different excitation regimes

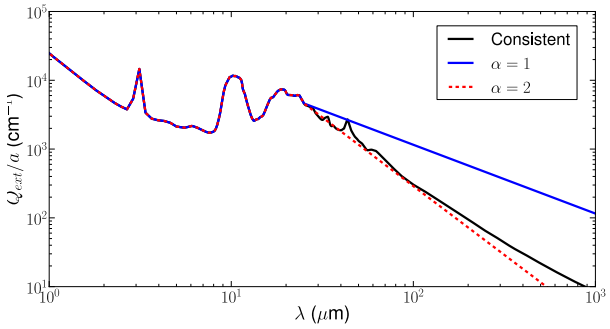

Fig. 2. Dust extinction efficiencies divided by grain size (in cm^{-1}) versus wavelength (in μm) used for the models shown in Figs. 3 and 4. At $\lambda < 25$ μm the profiles are identical. From 25 μm onward, the blue full line and the red dashed line show a profile where the region at $\lambda > 25$ μm is replaced with a power law of the form $Q_{\rm ext}/a \sim \lambda^{-\alpha}$ assuming $\alpha = 1$ and $\alpha = 2$, respectively. The black full line is representative of a typical oxygen-rich OH/IR extinction profile as used in MCMax, for which the dust composition is given in Table 3.

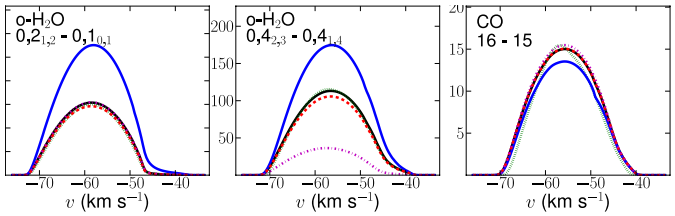

Fig. 3. Line profile predictions for the high mass-loss-rate case $\dot{M}_{\rm g} = 5.0 \times 10^{-5}$ $M_\odot$ yr^{-1}. The full black curve corresponds to the standard model with the inner radius of the gas shell $R_{\rm i,g} = 3$ $R_\star$, the black extinction efficiency profile from Fig. 2 and $\psi = 0.01$. In all other models only a single property is modified. The dotted green curve (which coincides with the other curves) assumes $R_{\rm i,g} = 10$ $R_\star$, the full blue and dashed red curves apply the blue and red extinction efficiency profiles from Fig. 2 and the dashed-dotted magenta curve assumes $\psi = 0.001$ (see Sect. 3.6 for more details).

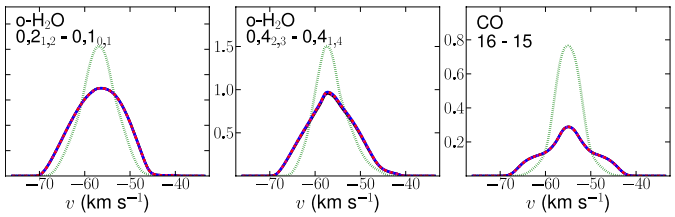

Fig. 4. As Fig. 3, with $\dot{M}_{\rm g} = 1.0 \times 10^{-7}$ $M_\odot$ yr^{-1}. All but the dotted green curve coincide.

accessible in the PACS wavelength domain, we use a standard input template (Table 1) and vary one parameter at a time. We give an overview for high ($\dot{M}_{\rm g} \sim 5.0 \times 10^{-5}$ $M_\odot$ yr^{-1}) and low ($\dot{M}_{\rm g} \sim 1.0 \times 10^{-7}$ $M_\odot$ yr^{-1}) mass-loss rates of the most significant effects including the condensation radius, the dust extinction efficiency profile, and the dust-to-gas ratio. For simplicity, we assume a power law for the gas temperature profile corresponding to Model 1 in Table 4. The extinction efficiency profiles under consideration are shown in Fig. 2. We present profiles for the CO $J = 16-15$ transition and the H_2O $2_{1,2}-1_{0,1}$ and $4_{2,3}-4_{1,4}$ transitions, all in the vibrational ground state. Figure 3 displays the high mass-loss-rate case, and Fig. 4 the low mass-loss-rate case. We discuss the effects below.

3.6.1. The condensation radius

In the high mass-loss-rate case, the condensation radius is not expected to have a strong influence on the theoretical line profiles thanks to the high opacity of the envelope. Indeed, the full black (condensation radius $R_{\rm i,g} = 3$ $R_\star$) and dotted green ($R_{\rm i,g} = 10$ $R_\star$) models coincide in Fig. 3 and the transitions have a parabolic line profile typical for optically thick winds. The lines shown here are formed at $r > 20$ $R_\star$ when the wind has already been fully accelerated, i.e. farther from the stellar surface than the condensation radius used for the green model.

In the low mass-loss-rate case, the line formation regions of the lines discussed here are located in the dust condensation region and the acceleration zone. Increasing the condensation radius in the low mass-loss rate model results in the removal of a relatively large amount of dust and effectively moves the acceleration zone outward. This manifests itself in the shape of the line profile. In the green model ($R_{\rm i,g} = 10$ $R_\star$) in Fig. 4, the line formation regions are located where the wind is accelerated. As a result, the lines exhibit a narrow Gaussian profile (Bujarrabal & Alcolea 1991; Decin et al. 2010a). In the black standard model, a narrow and a broad component are visible in the CO line, indicating that the line is formed both in a region where the wind is still being accelerated, and in a region where the wind has reached its terminal gas velocity. The H_2O $2_{1,2}-1_{0,1}$ line, however, is only formed in the part of the wind that has just reached the terminal gas velocity and leans toward a parabolic profile typical for an optically thick wind tracing only the terminal velocity. Even though dust is unimportant for the excitation of CO, its indirect influence through the optical depth of the inner region of the envelope highlights the importance of dust formation sequences and of the stellar effective temperature, which are often poorly constrained.

3.6.2. The dust opacity law

Often, the dust extinction efficiency profile is approximated by a power law, $Q_{\rm ext} \sim \lambda^{-\alpha}$, especially at wavelengths $\lambda > 25$ μm. Lamers & Cassinelli (1999) propose $\alpha \sim 2$, while Justtanont & Tielens (1992) suggest $\alpha \sim 1$ up to 1.5. Tielens & Allamandola (1987) propose to use $\alpha \sim 2$ for crystalline grains and $\alpha \sim 1$ for amorphous grains. An AGB envelope is usually dominated by amorphous material (up to at least 80% of the dust is amorphous, e.g. de Vries et al. 2010). However, Fig. 2 shows that $\alpha = 2$ is a better approximation of the dust extinction efficiency profile as calculated with MCMax for OH 127.8+0.0.

Comparing the three theoretical profiles for the high mass-loss rate case indicates the importance of the dust extinction efficiency profiles. This is expected because these efficiencies determine the thermal emission characteristics of the grains. The relative change of an H_2O line depends not only on the opacity law, but also on where the line is formed in the wind and on the spectroscopic characteristics of the line; i.e., for different excitation frequencies the dust radiation field will have a different effect. It is not straightforward to predict how these changes will show up for given assumptions about the dust extinction efficiency profile. If the excitation includes channels at wavelengths $\lambda \sim 10-200$ μm (i.e. excitation mechanism 3), H_2O excitation is very sensitive to the properties of the dust grains in the CSE. At low mass-loss rates, however, the dust content is too low for this mechanism to contribute significantly, such that H_2O excitation is controlled by the stellar radiation field in the near-IR (i.e. excitation mechanism 2).

Table 2. Modeling results for OH 127.8+0.0, associated with Model 2 in Table 4.

Modeling results			
$T_\star$	3000 K	$\psi_{\rm mom}$	$\geq 0.05 \times 10^{-2}$
$R_{\rm i,d} = R_{\rm i,g}$	$7.0\ R_\star$	$\psi_{\rm dens}$	1.0×10^{-2}
$R_{\rm o,g}$	$50 \times 10^3\ R_\star$	$\psi_{\rm H_2O}$	$\leq 0.5 \times 10^{-2}$
$R_{\rm o,d}$	$7 \times 10^3\ R_\star$	$N_{\rm H_2O-ice}$	3.9×10^{17} cm^{-2}
$\dot{M}_{\rm g}$	$5 \times 10^{-5}\ M_\odot$ yr^{-1}	OPR	3
$\dot{M}_{\rm d}$	$5 \times 10^{-7}\ M_\odot$ yr^{-1}	$n_{\rm H_2O,crit}/n_{\rm H_2}$	1.7×10^{-4}
$v_{\infty,\rm d}$	13.6 km s^{-1}		

Notes. $T_\star$ gives the stellar effective temperature; $R_{\rm i,d}$ and $R_{\rm i,g}$ the dust and gas inner radii respectively; $R_{\rm o,g}$ the photodissociation radius of ^{12}CO; $R_{\rm o,d}$ the dust outer radius; $\dot{M}_{\rm d}$ and $\dot{M}_{\rm g}$ the dust and gas mass-loss rates; $v_{\infty,\rm d}$ the dust terminal velocity; $\psi_{\rm mom}$, $\psi_{\rm dens}$ and $\psi_{\rm H_2O}$ the dust-to-gas ratios derived from three different methods (see Sect. 3.5.3); $N_{\rm H_2O-ice}$ the H_2O ice column density; OPR the ortho-to-para H_2O ratio; and $n_{\rm H_2O,crit}/n_{\rm H_2}$ the critical H_2O vapor abundance with respect to H_2.

3.6.3. The dust-to-gas ratio

At high mass-loss rates, the sensitivity of H_2O excitation to the dust properties becomes very clear when comparing the low and high dust-to-gas ratio models in Fig. 3. To demonstrate this sensitivity, we consider first the H_2O $4_{2,3}$–$4_{1,4}$ line. The excitation mechanism for the H_2O $4_{2,3}$ level involves first absorbing photons at $\lambda \sim 273\ \mu$m, where the dust radiation field is weak, and subsequently at $\lambda \sim 80\ \mu$m, where the dust radiation field dominates. Decreasing the dust-to-gas ratio implies that fewer photons are available for the channel at $\lambda \sim 80\ \mu$m, decreasing the population of the $4_{2,3}$ level. As a result, the strength of the H_2O $4_{2,3}$–$4_{1,4}$ emission line is decreased significantly. Populating the H_2O $2_{1,2}$ level, on the other hand, only involves channels at $\lambda \sim 180\ \mu$m, where the dust radiation field is again weak. As a result, the H_2O $2_{1,2}$–$1_{0,1}$ line is not affected by a decrease in the dust-to-gas ratio.

Both H_2O lines are affected by a change in the dust extinction efficiency profile. A profile with a different slope ($\alpha = 1$ as opposed to $\alpha = 2$ in this example, see Fig. 2) results in a relatively stronger dust radiation field at wavelengths $\lambda > 150\ \mu$m as compared with the dust radiation field at $\lambda \sim 80\ \mu$m. As a result, both H_2O lines are affected because the dust radiation field becomes stronger with respect to the underlying stellar and interstellar background radiation field at $\lambda > 150\ \mu$m. CO emission is not noticeably affected when changing the dust-to-gas ratio, indicating that collisional excitation dominates for this molecule.

Ultimately, if collisions are not energetic enough to have a significant impact, it is the balance between 1) the dust; 2) the stellar, and 3) the interstellar background radiation fields at all wavelengths involved in populating a given excitation level that will determine the effect of different dust properties on molecular line strengths.

4. Case study: the OH/IR star OH 127.8+0.0

We applied the combined modeling with GASTRoNOoM and MCMax to the OH/IR star OH 127.8+0.0. Table 2 gives the modeling results, which are discussed in this section.

4.1. Thermal dust emission

To model the IR continuum of OH 127.8+0.0, we followed the five-step approach presented in Sect. 3.3. With the assumed parameters listed in Table 1, there are few parameters left to adapt in order to reproduce the observed IR continuum. The inner radius $R_{\rm i,d}$ was fixed by considering pressure-dependent dust condensation temperatures. The stellar effective temperature $T_\star$ has no influence on the IR continuum of the dust due to the high optical depth of the wind of OH 127.8+0.0 and is constrained to some extent by the CO emission modeling. The dust terminal velocity $v_{\infty,\rm d}$ was derived from the momentum transfer between gas and dust.

This only leaves the dust-mass-loss rate $\dot{M}_{\rm d}$, the outer radius of the dust shell $R_{\rm o,d}$, and the dust composition as free parameters for fitting the thermal dust emission features and the overall shape of the IR continuum. The parameter $R_{\rm o,d}$ was chosen such that the emergent flux at long wavelengths matches the PACS data well, in agreement with the model suggested by Kemper et al. (2002). Sylvester et al. (1999) show that the spectral features in the 30 to 100 μm range can be reproduced by a combination of amorphous silicates, forsterite, enstatite, and crystalline H_2O ice. Following Kemper et al. (2002), metallic iron was also included. The theoretical extinction coefficients of amorphous silicate were calculated from a combination of amorphous olivines with different relative magnesium and iron fractions, determined by modeling the dust features in the IR continuum of the O-rich AGB star Mira (de Vries et al. 2010). The dust species and their condensation temperatures, as well as their mass fractions, are listed in Table 3. The dust-mass fractions are given in terms of mass density of the dust species with respect to the total dust-mass density, assuming all six modeled dust species have been formed. Figure 5 shows the temperature profiles of each dust species. Also shown is the average dust temperature profile $T_{\rm d,avg}$ that is adopted as the input dust-temperature profile for GASTRoNOoM in our five-step approach. Our results for the dust composition agree well with those of Kemper et al. (2002). We find a higher forsterite abundance and slightly higher metallic iron abundance, whereas the amorphous silicate abundance is lower. These differences are minor.

The mass fraction of crystalline and amorphous H_2O ice is determined by fitting the 3.1 μm absorption feature in the continuum-divided ISO-SWS data, see Fig. 6. The slightly shifted peak position around 3.1 μm in the mass extinction coefficients of amorphous and crystalline ice allows one to reproduce the shape and strength of this absorption feature. We find a crystalline to amorphous H_2O ice ratio of 0.8 ± 0.2 and a total relative mass fraction of (16 ± 2)% for H_2O ice, which leads to a radial column density of $N_{\rm H_2O-ice} = (3.9 \pm 0.5) \times 10^{17}$ cm^{-2}.

Sylvester et al. (1999) and Kemper et al. (2002) have modeled the IR continuum of OH 127.8+0.0 extensively. Using only crystalline H_2O ice, they find $N_{\rm H_2O-ice} = 5.5 \times 10^{17}$ cm^{-2} and $N_{\rm H_2O-ice} = 8.3 \times 10^{17}$ cm^{-2}, respectively. Dijkstra et al. (2006) have done a theoretical study of H_2O ice formation (Dijkstra et al. 2003) to calculate the expected H_2O ice mass fractions in OH/IR stars. For a CSE with parameters similar to what we find for OH 127.8+0.0, they expect that only 2% of the total dust mass is H_2O ice, which is a factor of 5 lower than the Kemper et al. (2002) results and a factor of 8 lower than our results. However, they assumed an initial H_2O vapor abundance of 1×10^{-4} in their H_2O ice formation models, which is a rather low estimate for an OH/IR star (Cherchneff 2006). More H_2O vapor may lead to the formation of more H_2O ice and would be more in line with our results. Moreover, following their H_2O ice formation models, Dijkstra et al. (2006) show that no strong H_2O ice features are expected in the IR continuum at 43 μm and 62 μm because most of the H_2O ice is predicted to be amorphous. Unlike this theoretical result, they point to significant

Table 3. Dust composition of OH 127.8+0.0 's CSE.

Dust species	Chemical formula	ρ_s (g cm^{-3})	T_{cond} (K)	$\rho_{species}/\rho_d$ (%)	Reference
Amorphous silicate	$(Mg_xFe_{1-x})_2SiO_4$	3.58	1100	69	1
Enstatite	$MgSiO_3$	2.80	950	3	2
Forsterite	Mg_2SiO_4	3.30	950	7	3
Metallic iron	Fe	7.87	1150	5	4
Crystalline water ice	c-H_2O	1.00	110	7	5
Amorphous water ice	a-H_2O	1.00	100	9	5, 6

Notes. Listed are the dust species with their chemical formula, their specific density ρ_s, the condensation temperature T_{cond}, the mass fraction of the dust species (given as the mass density of the dust species with respect to the total dust-mass density $\rho_{species}/\rho_d$, assuming all dust species have been formed), and the reference to the optical data for the opacities. The references for the optical constants of the dust species are as follows: 1) de Vries et al. (2010) and references therein; 2) Jäger et al. (1998); 3) Servoin & Piriou (1973); 4) Henning & Stognienko (1996); 5) Warren (1984); 6) Bertie et al. (1969).

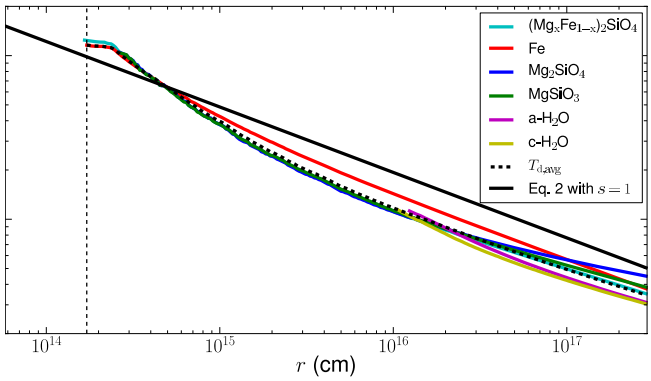

Fig. 5. Dust-temperature profiles for OH 127.8+0.0 as modeled with MCMax. The full colored lines indicate the specific dust species: cyan for amorphous silicates, red for metallic iron, blue for forsterite, green for enstatite, magenta for amorphous H_2O ice, and yellow for crystalline H_2O ice. Each of these profiles are cut off at the condensation temperature. The dashed black line gives the mean dust temperature profile. The full black line shows the power law from Eq. (2), with $s = 1$. The vertical dashed line indicates the inner radius of the dust shell.

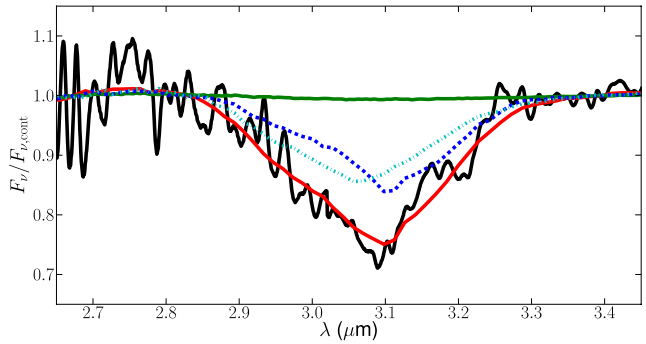

Fig. 6. 3.1 μm ice absorption feature. The continuum-divided ISO-SWS data are shown in black. The red curve gives the best fit model and the green curve gives the model without H_2O ice. The dashed blue and dotted cyan curve give the contributions from crystalline and amorphous H_2O ice, respectively.

fractions of crystalline H_2O ice in the spectra of many sources, in agreement with the large crystalline fraction that we find for OH 127.8+0.0. They suggest several explanations for this behavior, including a high mass-loss rate over luminosity ratio, axisymmetric mass loss, and clumpiness of the wind, all of which were not taken into account in their ice formation models.

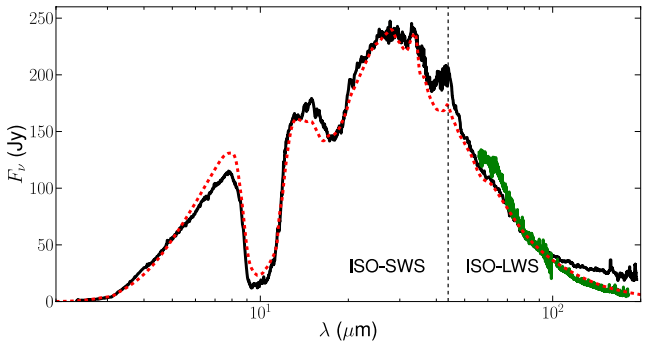

Fig. 7. SED of OH 127.8+0.0. In black the combined ISO-SWS and LWS data are shown; in green the PACS data are given. The dashed red curve is our best-fit model. The vertical dashed black line indicates the transition between the ISO-SWS and ISO-LWS data.

For the dust composition described above we find a dust-mass-loss rate of $\dot{M}_d = (5.0 \pm 1.0) \times 10^{-7}\ M_\odot\ \mathrm{yr}^{-1}$. This agrees well with results previously obtained: $\dot{M}_d = 4.0 \times 10^{-7}\ M_\odot\ \mathrm{yr}^{-1}$ by Suh (2004) and $\dot{M}_d = (7 \pm 1) \times 10^{-7}\ M_\odot\ \mathrm{yr}^{-1}$ by Kemper et al. (2002), both assuming spherical dust grains. The use of the CDE particle-shape model results in higher extinction efficiencies relative to spherical particles (Min et al. 2003), in principle implying the need for less dust to fit the IR continuum of the dust. The choice of particle model does not significantly influence the relative mass fractions of the dust species. The resulting SED model, as well as the data, is shown in Fig. 7. We lack some IR continuum flux in the region 40 μm $< \lambda <$ 70 μm in our model, which is a problem that has been indicated by previous studies of OH/IR stars, e.g. Kemper et al. (2002) and de Vries et al. (2010).

4.2. Molecular emission

We focus here on modeling the CO and H_2O emission lines. Apart from these molecules, notable detections in the PACS spectrum concern OH emission at $\lambda \sim 79.1$ μm, ~98.7 μm and ~162.9 μm. The line strengths of these emission lines are listed in Table A.1. Because the OH emission occurs in doublets, the line strengths of both components have been summed. We refer to Sylvester et al. (1997) for details on OH spectroscopy. These detections agree with the OH rotational cascade transitions involved in some of the far-IR pumping mechanisms suggested as being responsible for the 1612 MHz OH maser (Elitzur et al. 1976; Gray et al. 2005). Additional OH rotational

cascade transitions are expected in the PACS wavelength range at $\lambda \sim 96.4$ μm and ~119.4 μm, but they are not detected. These results are in accordance with Sylvester et al. (1997), who have searched for the 1612 MHz OH maser channels in the ISO data of the yellow hypergiant IRC+10420. The three strongest emission lines were found at the same wavelengths as our OH detections, while the two other rotational cascade lines in the PACS wavelength range were significantly weaker, if detected at all. To our knowledge, this is the first detection of the 1612 MHz OH maser formation channels in the far-infrared in an AGB CSE. Owing to the complexity of maser formation and the spectroscopy of OH, however, we do not include these OH emission lines in the analysis.

4.2.1. CO emission

We assume that the dust-to-gas momentum transfer initiates the stellar wind at the inner radius $R_{\rm i,d}$ of the dust shell derived from the pressure-dependent dust condensation temperatures (see Sect. 4.1). The outer radius $R_{\rm o,g}$ of the gas shell is taken as equal to the photodissociation radius of CO, following the formalism of Mamon et al. (1988). This leaves the gas-mass-loss rate $\dot{M}_{\rm g}$, the stellar effective temperature $T_\star$, and the gas kinetic temperature profile $T_{\rm g}(r)$ as free parameters to model the CO emission lines.

In the five-step approach, the thermodynamics of the gas shell can be calculated consistently for steps 2 and 4. If the H_2O vapor abundance is high ($n_{H_2O}/n_{H_2} > 10^{-6}$), H_2O cooling becomes one of the dominant processes in the gas thermodynamics (Decin et al. 2006). This introduces a significant uncertainty in the gas-temperature profile if the H_2O vapor abundance is not well constrained. We therefore opt to parametrize the temperature structure. Using a grid calculation for several temperature structures and for a wide range of gas-mass-loss rates, we constrain $T_{\rm g}(r)$ empirically for OH 127.8+0.0. The grid probes five free parameters: the gas-mass-loss rate, ranging from 1.0×10^{-5} $M_\odot$ yr^{-1} to 2.0×10^{-4} $M_\odot$ yr^{-1}; the stellar effective temperature, ranging from 2000 K to 3500 K; and the gas kinetic temperature profile, which is approximated by a two-step power law of the form $T_{\rm g,1}(r) = T_\star\ r^{-\epsilon_1}$ for $r \leq R_{\rm t}$ and $T_{\rm g,2}(r) = T_{\rm g,1}(R_{\rm t})\ r^{-\epsilon_2}$ for $r \geq R_{\rm t}$. We vary ϵ_1 and ϵ_2 from 0.0 to 1.1 and the transition radius $R_{\rm t}$ from 5 $R_\star$ to 50 $R_\star$. A power law with $\epsilon = 0.5$ for the gas kinetic temperature is expected for optically thin regions (Decin et al. 2006), but we allow for significantly steeper laws as well in view of the high optical depth in OH 127.8+0.0's CSE.

We use the spectrally resolved low-J CO transitions observed with JCMT and HIFI to constrain the free parameters. Following Decin et al. (2007), the evaluation of the model grid is done in two steps. First, all models that do not agree with the absolute flux calibration uncertainties $\sigma_{\rm abs}$ on the data sets, as specified in Sect. 2, are excluded. Then, a goodness-of-fit assessment based on the log-likelihood function is set up to judge the shape of the line profile, taking statistical noise $\sigma_{\rm stat}$ into account. For this last step, a scaling factor is introduced to equalize the integrated intensity of the observed line profile with the integrated intensity of the predicted line profile. The JCMT data do not significantly detect the CO $J = 6-5$ transition. We use both the $3\sigma_{\rm stat}$ noise level and $\sigma_{\rm abs}$ to define an upper limit for the predicted intensities of this line. We also compare the predicted line profiles of the CO $J = 2-1$ and $J = 3-2$ JCMT observations with the soft parabola component of the fitted line profile, rather than the observed line profile, in which the interstellar CO contamination does not allow for a reliable determination of the integrated intensity and the line profile shape.

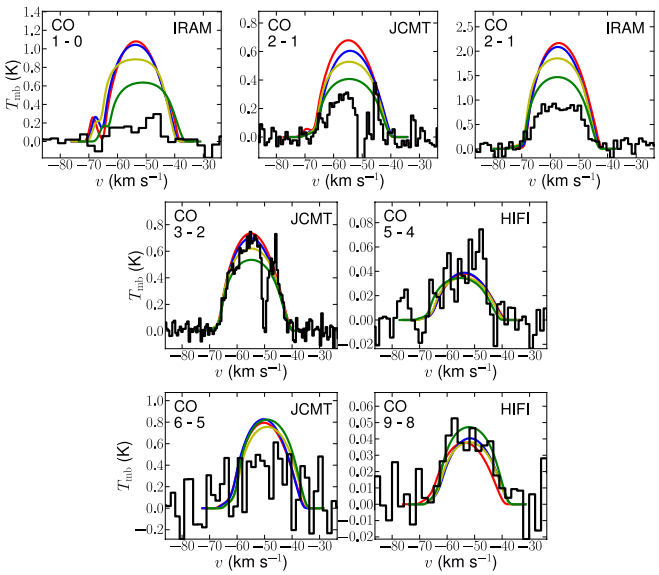

Fig. 8. Spectrally resolved low-J CO observations of OH 127.8+0.0 are shown in black. The colored curves correspond to the models listed in Table 4, which assume a constant mass-loss rate: 1. red; 2. blue; 3. yellow; 4. green. See Sect. 4.2.2 for further discussion of the validity of these CO models.

Table 4. Values for the grid parameters of the four best fit models to the CO molecular emission data.

	$T_\star$ (K)	ϵ_1	ϵ_2	$R_{\rm t}$ ($R_\star$)	$\dot{M}_{\rm g}$ ($M_\odot$ yr^{-1})	$\psi_{\rm dens}$	$n_{\rm H_2O,crit}/n_{\rm H_2}$
1	3500	0.2	0.9	5	1.0×10^{-4}	0.005	8.5×10^{-5}
2	3000	0.2	0.9	5	5.0×10^{-5}	0.01	1.7×10^{-4}
3	2500	0.2	0.9	5	2.0×10^{-5}	0.025	4.0×10^{-4}
4	2000	0.01	1.0	5	2.0×10^{-5}	0.025	4.0×10^{-4}

Notes. Listed are the stellar effective temperature $T_\star$, the powers of the 2-step power law ϵ_1 and ϵ_2, the transition radius $R_{\rm t}$, the gas-mass-loss rate $\dot{M}_{\rm g}$, the dust-to-gas-ratio $\psi_{\rm dens}$, and the critical H_2O abundance $n_{\rm H_2O,crit}/n_{\rm H_2}$.

With the exception of the CO $J = 1-0$ and $J = 2-1$ observations, four models reproduce all of the available CO transitions, shown in Fig. 8. Our estimate of the uncertainty on the mass-loss rates given in Table 4 amounts to a factor of three on the given values and is dominated by the sampling resolution of the mass-loss-rate parameter in the model grid, as well as by the uncertainty of the CO abundance that we assume. These values compare well with the mass-loss-rate estimates of $\dot{M}_{\rm g} \sim 5 \times 10^{-5}$ $M_\odot$ yr^{-1} reported in the two most recent studies that included OH 127.8+0.0 (Suh & Kim 2002; De Beck et al. 2010). Because the CO lines in the PACS wavelength region are undetected, the PACS data only provide an upper limit for the high-J CO emission lines. All models listed in Table 4 agree with this upper limit.

4.2.2. Validity of CO model results

Model 1 in Table 4 requires a stellar effective temperature of 3500 K, which is comparatively high for OH/IR stars. Owing to the high optical thickness of the circumstellar shells in OH/IR stars, the common method of deriving stellar effective

temperatures based on $V-K$ color measurements cannot be used to constrain the effective temperature (De Beck et al. 2010). Lepine et al. (1995) have attempted to constrain the effective temperatures for a large sample of OH/IR stars based on near-IR ($K-L'$) colors. They find temperatures lower than 3000 K for the whole sample, contrasting with the value found for our Model 1. We choose not to exclude Model 1 because of the uncertainty involved in determining effective temperatures for sources with optically thick shells.

All predictions in Table 4 overestimate the CO $J = 2-1$ observations by a factor 1.5 up to 3 and the CO $J = 1-0$ line by a factor of 3 up to 5. Two explanations are possible:

1. The CO $J = 1-0$ and $J = 2-1$ lines are formed in the outermost part of the CSE, where the contribution of the interstellar radiation field cannot be neglected. This radiation field depends strongly on the local conditions. For instance, if a strong UV-source is present near OH 127.8+0.0, the photodissociation radius of CO determined from the general formalism derived by Mamon et al. (1988) would decrease. Reducing $R_{o,g} \sim 50 \times 10^3\ R_\star$ to $R_{o,g} \sim 1500-2000\ R_\star$ would allow the model to predict the observed intensity of the CO $J = 1-0$ and $J = 2-1$ lines correctly, while keeping the intensity of the higher-J lines the same. However, this is remarkably close to the radius of the OH 1612 MHz maser shell in OH 127.8+0.0, which Bowers & Johnston (1990) found to be $(1.38 \pm 0.14)''$. This translates to $r_{OH} \sim 1000-2000\ R_\star$ at a distance of 2.1 kpc, depending on the assumed temperature at the stellar surface. This suggests that such a small outer CSE radius is unlikely for OH 127.8+0.0.
2. The mass loss in OH 127.8+0.0 may be variable, as suggested by several previous studies (e.g. De Beck et al. 2010). If the mass-loss rate has been lower in the past, then the low-J lines might have a lower intensity compared to our predictions assuming a constant mass-loss rate. To improve the prediction of the $J = 1-0$ and $J = 2-1$ CO lines, we calculated models with a change in mass-loss rate going from $\dot{M}_g = 1 \times 10^{-7}\ M_\odot\ yr^{-1}$ in the outer wind up to $\dot{M}_g$ as listed in Table 4 for the inner wind. The transition from high to low mass-loss rate occurs gradually at the radial distance R_{VM} of ~2500–4000 $R_\star$, which translates to $\sim 7.5-14.5 \times 10^{16}$ cm. Delfosse et al. (1997) found similar results based on the IRAM ^{12}CO and ^{13}CO $J = 2-1$ and $J = 1-0$ transitions with an older, low mass-loss rate of $\dot{M}_{g,l} < 5 \times 10^{-6}\ M_\odot\ yr^{-1}$ and a recent, high $\dot{M}_{g,h}$ between 5×10^{-5} and $5 \times 10^{-4}\ M_\odot\ yr^{-1}$. They found a transitional radius of $R_{VM} \sim 1.8-5.3 \times 10^{16}$ cm, depending on $\dot{M}_{g,h}$. Our estimate of R_{VM} is larger, but we have a stronger constraint on R_{VM} due to the higher-J CO transitions. The values we find for R_{VM} translate to an increase in the mass-loss rate in OH 127.8+0.0 in the last 2000 up to 4000 years, depending on $\dot{M}_{g,h}$ and the temperature structure. This recent change in mass-loss rate is commonly referred to as the recent onset of the superwind, which is often suggested for many OH/IR stars by several studies (Justtanont & Tielens 1992, Delfosse et al. 1997; de Vries et al., in prep; Justtanont et al., in prep.).

The assumption of a change in mass-loss rate to predict the low-J CO line strengths correctly does not affect further modeling of other emission lines, as long as these lines originate in a region within the radial distance R_{VM}. This is the case for the H_2O vapor emission lines detected in the PACS wavelength range, so we use the four models listed in Table 4 in what follows.

4.2.3. H_2O emission

To determine the H_2O vapor abundance, we use ψ_{dens} and adopt the gas kinetic temperature law and gas-mass-loss rate of Model 2 in Table 4 because the mass-loss rate is closest to the estimates of previous studies. What follows has been done for every model in Table 4, and even though the resulting values scale with the mass-loss rate, the general conclusions do not change.

We have selected 18 mostly unblended, non-masing H_2O emission lines in the PACS spectrum to fit the GASTRoNOoM models. The selection of lines is indicated in Table A.1. We assume an ortho-to-para H_2O ratio (OPR) of 3 (Decin et al. 2010b). When using $\psi_{dens} = 0.01$ derived from fitting CO emission and the thermal IR continuum (see Sect. 3.5.3) for Model 2 in Table 4, we find an unexpectedly low H_2O vapor abundance[3] $n_{H_2O}/n_{H_2} \sim 5 \times 10^{-6}$, as compared with $n_{H_2O}/n_{H_2} \sim 3 \times 10^{-4}$ derived from chemical models (Cherchneff 2006). Maercker et al. (2008) also found an H_2O vapor abundance of $\sim 10^{-6}$ for the OH/IR source WX Psc, indicating that such a discrepancy has been found before in sources that have a high mass-loss rate.

To resolve this discrepancy, we determine ψ_{H_2O} for a wide range of H_2O vapor abundances such that our model reproduces the H_2O emission spectrum of OH 127.8+0.0. The results for Model 2 in Table 4 are shown in Fig. 9 and give further clues to the excitation mechanism of H_2O vapor in the high mass-loss-rate case. At values $\geq 10^{-3}$, ψ_{H_2O} correlates with the H_2O vapor abundance. Here, pumping through excitation by the dust radiation field plays an important role. For lower dust-to-gas ratios, the dust radiation field becomes negligible for H_2O vapor excitation causing the correlation between ψ_{H_2O} and n_{H_2O}/n_{H_2} to level off. The correlation between ψ_{H_2O} and the H_2O vapor abundance depends on the gas-mass-loss rate. For comparison, equivalent results for Model 1 in Table 4 are shown in Fig. 9.

Figures 10 and 11 show the continuum-subtracted PACS spectrum compared to the predictions of Model 2 in Table 4 for $n_{H_2O}/n_{H_2} = 3 \times 10^{-4}$ and $\psi_{H_2O} = 0.003$. Included and indicated on the spectrum are all ^{12}CO rotational transitions in the vibrational groundstate and all o-H_2O and p-H_2O transitions in the vibrational groundstate and the $\nu_1 = 1$ and $\nu_2 = 1$ vibrational states with rotational quantum number up to $J_{upper} = 8$ in the PACS wavelength range, regardless of being detected or not. The 18 H_2O transitions used in the initial fitting procedure are indicated as well. We calculated model spectra for the other temperature and density profiles in Table 4 and arrive at the same overall result as for Model 2 with some small differences in the relative line strengths of the lines.

4.2.4. Validity of H_2O model results

A slight downward trend is present in the comparison between model predictions and the observations, as shown in Figs. 10 and 11, with a systematic overestimation at short wavelengths and a systematic underestimation at longer wavelengths. This difference is within the 30% absolute uncertainty calibration of the PACS data. However, a relative trend between short and long wavelengths in the model-to-data comparison is unexpected from the absolute calibration errors. A relative uncertainty between short and long wavelengths can be caused by pointing errors of the telescope, but this effect is likely too small to explain the trend that we find. This trend is present for all models

[3] H_2O vapor abundances are always given for ortho-H_2O alone, while H_2O column densities and H_2O ice abundances always include both ortho- and para-H_2O.

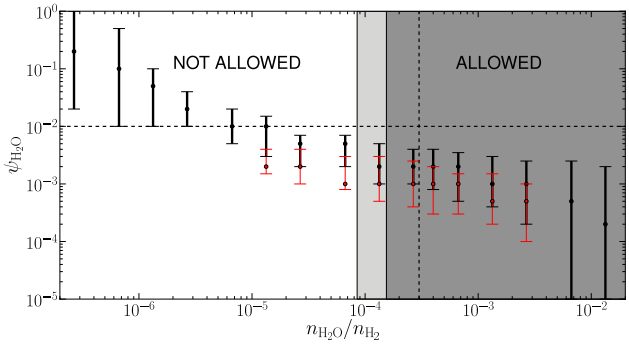

Fig. 9. OH 127.8+0.0 H_2O emission spectrum modeling results for the temperature law and mass-loss rate of Models 1 and 2 in Table 4 in red and black, respectively. ψ_{H_2O} and its uncertainty is determined for a wide range of (ortho + para) H_2O vapor abundances. From the modeling of the IR continuum and the CO data, a value of $\psi_{dens} = 0.01$ is determined. The expected H_2O vapor abundance from chemical models is 3×10^{-4} (Cherchneff 2006). Both values are indicated by the dashed black lines. The dark gray area indicates the lower limit defined by the critical H_2O vapor abundance derived from the H_2O ice fraction of Model 2, see Sect. 4.2.5. For comparison, the light gray area indicates the lower limit found for Model 1.

in Table 4, although less evident for Models 3 and 4 (with the lower mass-loss-rate estimate of $\dot{M}_g \sim 2 \times 10^{-5}\ M_\odot\ yr^{-1}$).

Based on this, one could opt to exclude Models 1 and 2. However, H_2O is not a good tracer of the density and temperature structure owing to the complexity of H_2O excitation mechanisms and possible maser effects. Normally, CO is a good density and temperature tracer, because CO is dominated by collisional excitation and does not mase. However, for OH 127.8+0.0, CO lines are optically thick and were not reliably detected in the PACS wavelength range. In this case, ^{13}CO lines would be a better tracer, but they are significantly weaker than ^{12}CO emission lines and, as such, are not detected at all in the PACS observations. As long as the majority of H_2O lines are reproduced well over a wide range of wavelengths in the PACS data, for which the signal-to-noise ratio is low especially at short wavelengths, we consider a model to be satisfying. Thus, we choose not to exclude any models based on the trend in the predictions.

This large a set of H_2O lines has not been modeled before in such detail, covering full radiative transfer modeling of the CSE of a high mass-loss-rate OH/IR star. The consistent prediction of line-integrated fluxes of H_2O lines across a wide wavelength range that is well within the absolute flux calibration of the PACS instrument – especially in the red bands – is remarkable, considering the large number of H_2O lines and the complexity of the problem.

4.2.5. The H_2O vapor-ice connection

An additional constraint can be placed on the estimate of the H_2O vapor abundance and the associated ψ_{H_2O}. The presence of H_2O ice in an OH/IR CSE provides a lower limit on the H_2O vapor abundance. The condensation temperature of H_2O ice is $T_{cond,ice} = 110$ K, following Kama et al. (2009). The condensation radius associated with 110 K is $R_{cond,ice} = 1.2 \times 10^{16}$ cm. The line formation region for all unblended, nonmasing H_2O vapor lines in the spectrum of OH 127.8+0.0 is mostly within this radius. We can therefore define a critical H_2O vapor abundance at $r < R_{cond,ice}$, below which there would not be enough H_2O vapor to form the observed amount of H_2O ice at $R_{cond,ice}$. Following our modeling of the H_2O ice feature, the H_2O ice column density at $r > R_{cond,ice}$ is 8.3×10^{17} cm^{-2}, which leads to a critical (ortho + para) H_2O vapor abundance of $n_{H_2O,crit}/n_{H_2} = (1.7 \pm 0.2) \times 10^{-4}$. This critical abundance depends on the gas-mass-loss rate, as the ice mass is compared to the equivalent molecular hydrogen mass in the ice shell. As such, this critical value will be different for the three mass-loss rates given in Table 4. For comparison, the critical H_2O vapor abundance is shown in Fig. 9 for Models 1 and 2 in Table 4. The work by Dijkstra et al. (2003) suggests that at most 20% of the H_2O vapor will freeze out onto dust grains. The actual H_2O vapor abundance is thus expected to be larger than the critical H_2O vapor abundance. Figure 12 gives a schematic representation of what the H_2O vapor abundance profile might look like, taking H_2O ice condensation into account (with a freeze-out of ~40%, a value that is arbitrarily chosen) and H_2O vapor photodissociation in the outer envelope.

Observational evidence of a larger actual H_2O vapor abundance than the critical H_2O vapor abundance is given by the presence of emission from the OH maser at 1612 MHz in a shell at $r > R_{cond,ice}$. The photodissociation of H_2O into OH and H is one of the main OH production paths, throughout the whole envelope, as long as interstellar UV radiation is available to break up H_2O molecules. Netzer & Knapp (1987) have shown that the OH abundance reaches a maximum at the radial distance where the OH maser shell at 1612 MHz is observed, indicating that other methods of OH production closer to the star, such as shock chemistry, can be ignored. As a result, H_2O needs to be present in the CSE at least up to the radial distance where the OH abundance peaks. In the case of OH 127.8+0.0, the radius of the OH 1612 MHz maser shell is $(1.38 \pm 0.14)''$ (Bowers & Johnston 1990), which translates to $r_{OH} = (4.3 \pm 0.4) \times 10^{16}$ cm at a distance of 2.1 kpc. Netzer & Knapp (1987) also give a formula for the expected OH 1612 MHz maser shell radius, which depends on the assumed interstellar radiation field (Habing 1968). Assuming the average Habing field, we find 6.1×10^{16} cm, whereas the high Habing field leads to a shell radius of 4.3×10^{16} cm.

Our results for the critical H_2O vapor abundance agree well with those found in other studies. Cherchneff (2006) derived the expected abundances for several molecules from thermodynamic equilibrium and shock-induced NLTE chemistry, and found $n_{H_2O}/n_{H_2} \sim 3.0 \times 10^{-4}$ in O-rich AGB stars. H_2O vapor abundances derived by Maercker et al. (2008) for most sources in their sample lie between $n_{H_2O}/n_{H_2} = 2.0 \times 10^{-4}$ and 1.5×10^{-3}. They do find a remarkably low H_2O vapor abundance of $\sim 10^{-6}$ for the OH/IR star WX Psc and offer two explanations: 1) H_2O ice formation depletes H_2O in gaseous form; and 2) H_2O lines may be formed in a region of a more recent, lower mass-loss rate. However, Maercker et al. (2008) use ψ_{dens} for their molecular emission modeling. Our modeling has indicated that ψ_{dens} leads to too low an H_2O abundance in OH 127.8+0.0 when compared to the H_2O ice content. Given that OH 127.8+0.0 and WX Psc are similar, their low value for the H_2O vapor abundance in WX Psc could also be the result of the use of ψ_{dens} as an estimate of the dust-to-gas ratio.

4.3. Discussion: the dust-to-gas ratio

The dust-to-gas ratio typical of AGB circumstellar environments is 0.005 (Whitelock et al. 1994). We derive different values depending on the method used (for Model 2 in Table 4):

1. We find $\psi_{dens} = 0.01$, accurate to within a factor of three, from IR continuum and CO molecular emission modeling.

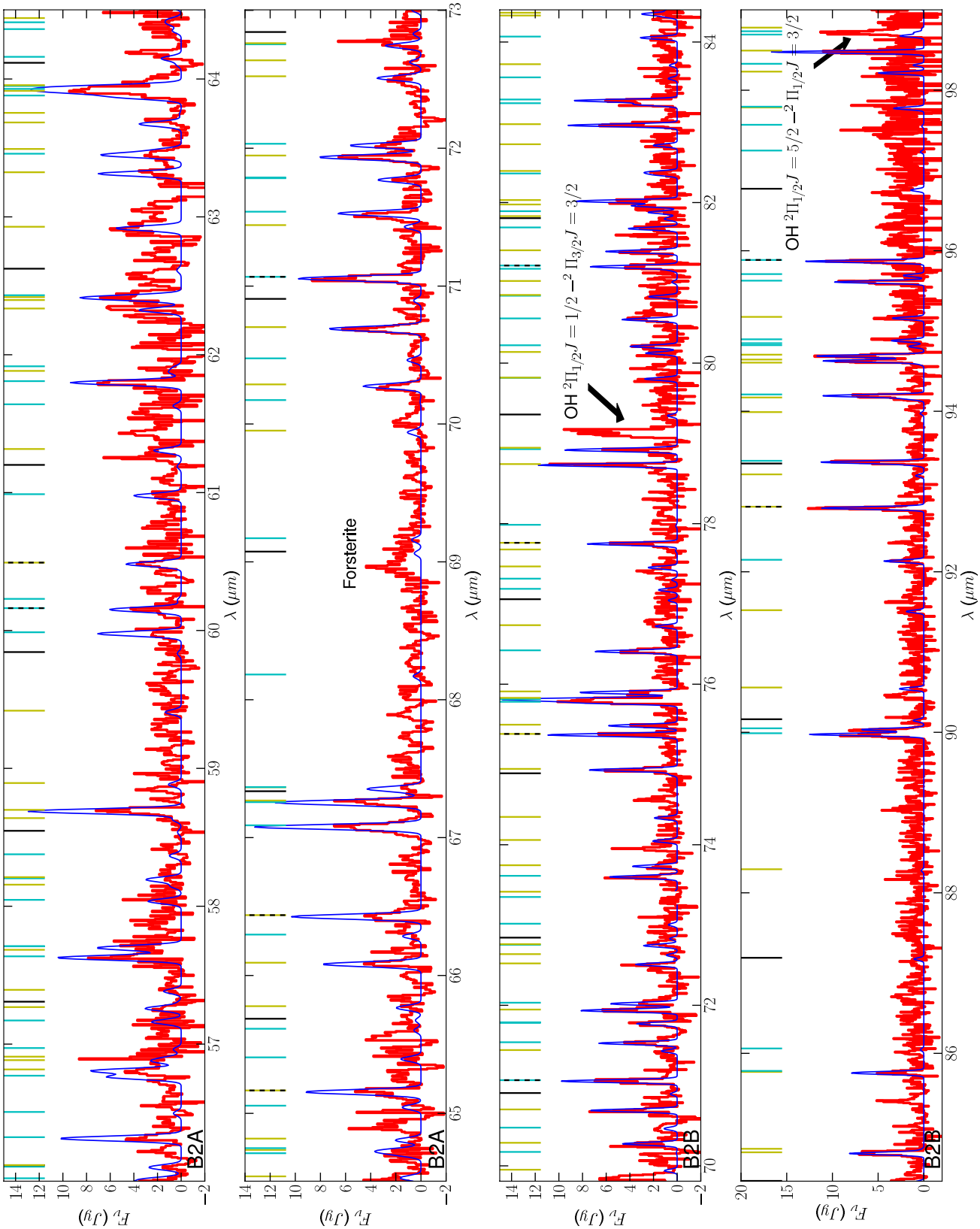

Fig. 10. Continuum-subtracted PACS spectrum of OH 127.8+0.0 is shown in red for the blue bands. The PACS band is indicated in the lower left corner of each spectrum. Model 2 in Table 4 with $n_{H_2O}/n_{H_2} = 3 \times 10^{-4}$ and $\psi_{H_2O} = 0.003$ is given in blue. The other parameters are listed in Tables 1 and 2. The colored vertical lines indicate the molecule contributing at that specific wavelength, with full black for ^{12}CO, yellow for ortho-H_2O, and cyan for para-H_2O. The dashed black-colored lines indicate the water lines used for the initial H_2O line fitting. The forsterite feature at ~69 μm (not completely removed during continuum subtraction) and the OH rotational cascade lines $^2\Pi_{1/2}J = 1/2 - ^2\Pi_{3/2}J = 3/2$ and $^2\Pi_{1/2}J = 5/2 - ^2\Pi_{1/2}J = 3/2$ at ~79.1 μm and ~98.7 μm, respectively, (not included in our modeling) are labeled.

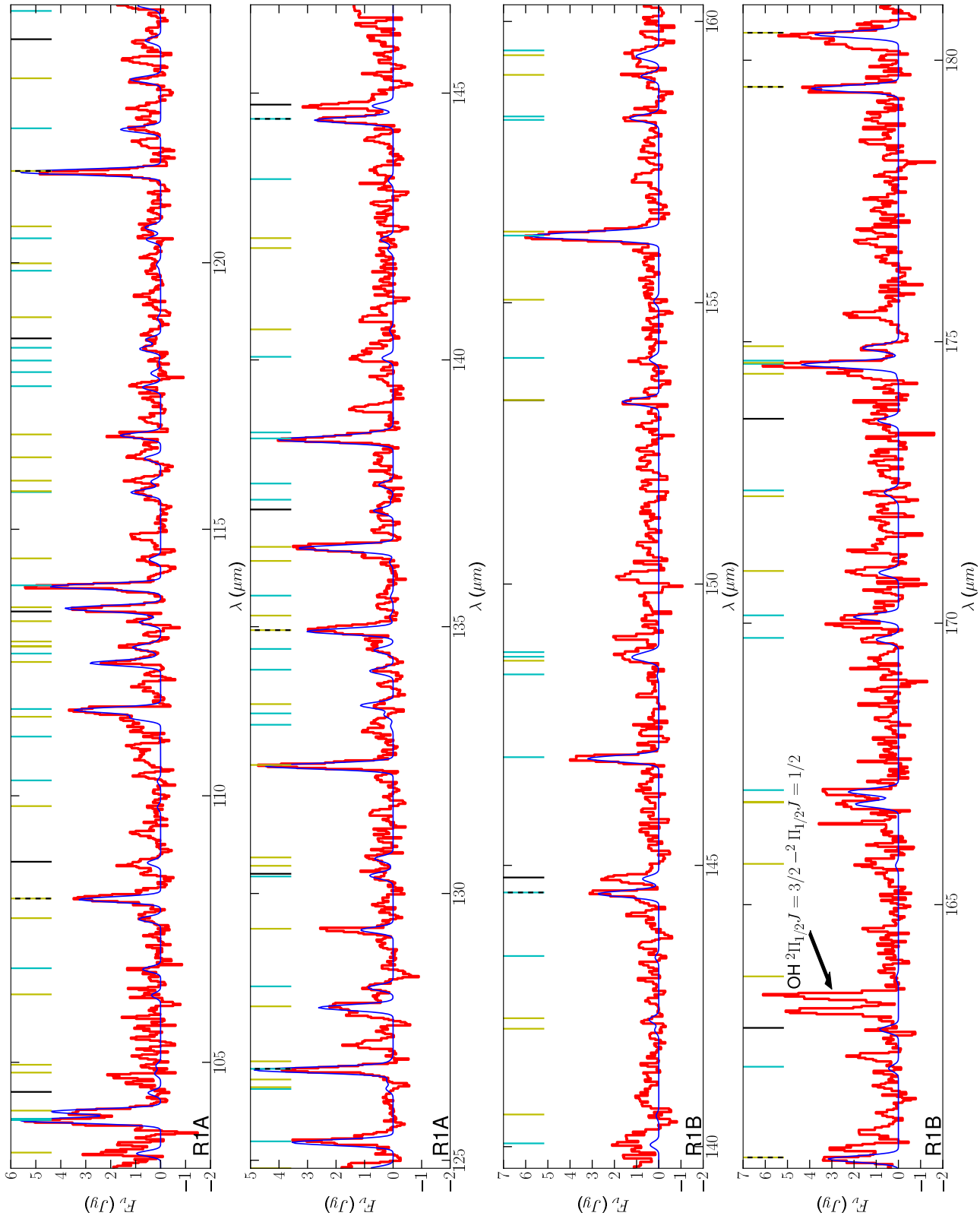

Fig. 11. Continuum-subtracted PACS spectrum of OH 127.8+0.0 is shown in red for the red bands. The PACS band is indicated in the lower left corner of each spectrum. Model 2 in Table 4 with $n_{H_2O}/n_{H_2} = 3\times10^{-4}$ and $\psi_{H_2O} = 0.003$ is given in blue. The other parameters are listed in Tables 1 and 2. The colored vertical lines indicate the molecule contributing at that specific wavelength, with full black for ^{12}CO, yellow for ortho-H_2O, and cyan for para-H_2O. The dashed black-colored lines indicate the water lines used for the initial H_2O line fitting. The OH rotational cascade line $^2\Pi_{1/2} J = 3/2 - ^2\Pi_{1/2} J = 1/2$ at ~162.9 μm (not included in our modeling) is labeled. At ~144.9 μm, another strong line appears both in band R1A and band R1B. A different wavelength sampling causes the line in band R1B to appear weaker, but the integrated line fluxes of both lines are within the absolute flux calibration uncertainty of PACS. This line remains unidentified. The CO line alone cannot explain the observed integrated line flux at this wavelength.

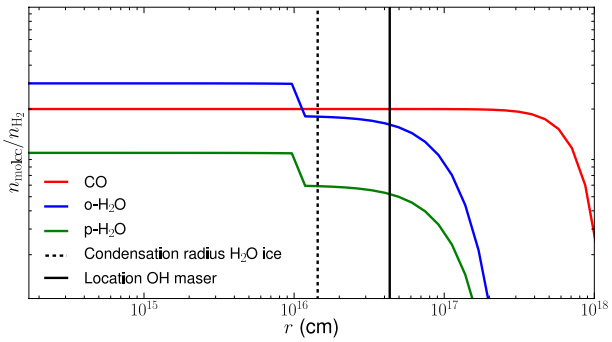

Fig. 12. Schematic representation of the CO (red), the ortho-H_2O (blue), and para-H_2O (green) abundance profiles. The vertical dashed black line indicates the H_2O ice condensation radius. The vertical full black line indicates the location of the OH 1612 MHz maser shell, assuming a distance of 2100 pc. The signal-to-noise of the PACS is too low to trace the drop in H_2O vapor abundance (shown here for a freeze-out of ~40%) at the H_2O ice condensation radius.

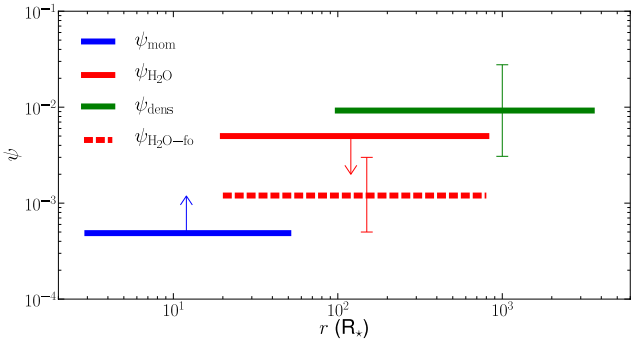

Fig. 13. Results of determining the dust-to-gas ratio using the three different methods described in Sect. 3.5.3 are shown for Model 2 in Table 4. The horizontal bar indicates the part of the envelope traced by the method. The vertical bar indicates the uncertainty on the indicated value. $\psi_{\rm mom}$ is a lower limit, whereas $\psi_{\rm H_2O}$ is an upper limit. For reference, the dashed red line indicates $\psi_{\rm H_2O-fo}$ assuming 20% freeze-out of H_2O vapor into H_2O ice. The relative differences between the three values of the dust-to-gas ratio for the other models in Table 4 are similar, but scale upward or downward uniformly depending on the gas-mass-loss rate. See Sect. 4.3 for a more detailed description.

2. The momentum transfer equation leads to a dust-to-gas ratio $\psi_{\rm mom} = 0.0005$, while assuming complete momentum coupling between dust and gas, i.e. dust grains of every grain size are coupled to the gas. For circumstellar environments typical of stars like OH 127.8+0.0, MacGregor & Stencel (1992) find that silicate grains with initial size smaller than ~0.05 μm decouple from the gas near the condensation radius. If the coupling is not complete, a higher dust content is required to arrive at the same kinematical structure of the envelope, implying that $\psi_{\rm mom} \geq 0.0005$.
3. The critical H_2O vapor abundance provides a strong constraint on the expected initial H_2O vapor abundance in OH 127.8+0.0. Applying our value of $n_{\rm H_2O,crit}/n_{\rm H_2} > 1.7 \times 10^{-4}$ to the grid calculation shown in Fig. 9, we find an upper limit for the associated dust-to-gas ratio $\psi_{\rm H_2O} < 0.005$. This upper limit takes the uncertainty shown in Fig. 9 into account and assumes the unlikely case of 100% freeze-out of H_2O vapor into H_2O ice. For reference, assuming a freeze-out of 20%, we arrive at $\psi_{\rm H_2O-fo} \sim 0.0015$, accurate to within a factor of two.

The results obtained for the dust-to-gas ratio appear incompatible. However, each method traces a different part of the envelope (see Fig. 13).

1. $\psi_{\rm dens}$ is based on modeling the thermal dust emission, which traces the dust content of the envelope out to a radius of ~5000 $R_\star$, and the CO $J = 9-8$ down to $J = 3-2$ emission lines. These lines are formed in the outer regions of the CSE at 100 $R_\star < r <$ 4000 $R_\star$, for Model 2 in Table 4. Assuming the dust-mass-loss-rate remains constant throughout the whole CSE, $\psi_{\rm dens}$ is therefore sensitive only to the outermost region of the envelope.
2. $\psi_{\rm mom}$ is determined from the momentum transfer equation and therefore traces the acceleration zone, which in our model is located at $r < 50\ R_\star$.
3. $\psi_{\rm H_2O}$ traces the outflow at 20 $R_\star < r <$ 800 $R_\star$ where all of the H_2O emission lines used to determine the H_2O abundance are formed.

As shown in Fig. 13, our findings tentatively point to the presence of a gradient in the dust-to-gas ratio with radial distance. The results shown here are for Model 2 in Table 4, but the same relative differences between the dust-to-gas ratio estimates are seen for the other models in Table 4. There could be several potential explanations for such behavior.

First, we assume a constant mass-loss rate for both the gas and dust components. If OH 127.8+0.0 's mass-loss history is not constant, a recent increase in the gas-mass-loss rate can explain the gradient in the dust-to-gas ratio only when the dust-mass-loss rate has not increased by the same factor as well. This is possible only if the dust forms less efficiently for an increased gas density. There is no immediate evidence that suggests such behavior for higher mass-loss rates, so this scenario appears to be unlikely.

Second, 84% of the dust mass is formed in the innermost region of the envelope, at a few stellar radii, and the dust-mass-loss rate is assumed to be constant. If dust formation extends beyond the vicinity of the dust condensation radius, this could explain the gradient in the dust-to-gas ratio. H_2O ice formation is possible at a radius of ~1000 $R_\star$ in the case of Model 2 in Table 4, owing to the high H_2O vapor abundance. However, the amount of H_2O ice formed is not enough to explain the radial increase in dust-to-gas ratio. Formation of other dust species (such as silicates) at large distances from the star is unlikely due to the lower densities of the precursor molecular species when compared to H_2O vapor.

Third, we do not take clumping into account in the models. If clumps are present in the envelope, the ones close to the stellar surface are likely to be much more optically thick than those in the outer envelope. As a result, we trace the real amount of gas and dust in the outer envelope, whereas we trace a seemingly lower amount of gas and dust in the inner envelope. If clumps are responsible for the gradient in the dust-to-gas ratio, we have to assume that the optical depth effect caused by clumping is more severe for dust than for gas. Considering that a cloud of gas particles experiences an internal pressure, whereas a cloud of dust particles does not, this could be a valid assumption. We note that a clumped wind is also invoked by Dijkstra et al. (2006) to explain the observed high crystalline H_2O ice fraction in OH 127.8+0.0.

5. Conclusions

We have combined two state-of-the-art radiative transfer codes, MCMax for the continuum radiative transfer, and GASTRoNOoM for the line radiative transfer. We justified the use of more consistent dust properties in the gas modeling by showing that the dust component of the CSE has a significant influence on the excitation of H_2O at high mass-loss rates, while the dust condensation radius is important for both CO and H_2O at low mass-loss rates.

We presented new PACS data of OH 127.8+0.0, the first AGB OH/IR star for which a far-IR spectrum was taken with this instrument. We applied our approach to the combination of the PACS spectrum, HIFI observations of two CO transitions taken in the framework of the SUCCESS Herschel Guaranteed Time Program, ground-based JCMT observations of low-J CO transitions, and the ISO-SWS and ISO-LWS spectra. The combination of the HIFI and ground-based observations suggests a discrepancy between the lowest-J ($J = 1{-}0$ and $J = 2{-}1$) and the higher-J ($J = 3{-}2$ and up) CO lines, which may point to a recent onset of a superwind in OH 127.8+0.0. The IR continuum is modeled with a dust composition of metallic iron, amorphous silicates, crystalline silicates (forsterite and enstatite), and amorphous and crystalline H_2O ice. We found a dust-mass-loss rate of $\dot{M}_{\rm d} = (5 \pm 1) \times 10^{-7}\ M_\odot\ {\rm yr}^{-1}$ and a contribution of H_2O ice to the total amount of dust beyond the H_2O ice condensation radius of $(16 \pm 2)\%$ with a crystalline-to-amorphous ratio of 0.8 ± 0.2. The CO transitions are modeled with an empirical temperature law resulting in four models with a constant gas-mass-loss rate ranging between $\dot{M}_{\rm g} = 1.0 \times 10^{-4}\ M_\odot\ {\rm yr}^{-1}$ and $\dot{M}_{\rm g} = 0.2 \times 10^{-4}\ M_\odot\ {\rm yr}^{-1}$, accurate to within a factor of three. The older mass-loss episode, traced by the outer regions of the CSE, is estimated to be $\dot{M}_{\rm g} \sim 1 \times 10^{-7}\ M_\odot\ {\rm yr}^{-1}$ with the transition between the low and high mass-loss rate occurring at $R_{\rm VM} \sim 2500{-}4000\ R_\star$. We derived a critical H_2O vapor abundance of $(1.7 \pm 0.2) \times 10^{-4}$ from the H_2O ice content of the CSE. This constrains the minimum amount of H_2O vapor required to produce the observed amount of H_2O ice assuming 100% freeze-out efficiency. We note that the comparison between H_2O vapor models and the PACS spectrum shows a flux overestimation at shorter wavelengths and a flux underestimation at longer wavelengths. Even though these differences are within the absolute flux calibration of the PACS instrument, the wavelength-dependent discrepancy cannot be explained.

We derived the dust-to-gas ratio following three methods, which are sensitive to different regions of the outflow. We found for the first time indications of a gradient in the dust-to-gas ratio with radial distance from the star. Possible explanations for this behavior can include clumpiness, variable mass loss, or continued dust growth beyond the condensation radius, of which the first suggestion seems the most likely.

Additionally, we reported the first detection in an AGB circumstellar environment of OH cascade rotational lines involved in the far-infrared pumping mechanism of the 1612 MHz OH maser.

Acknowledgements. We would like to thank B. Acke and A.J. van Marle for their contribution to the study. We also express gratitude toward the referee, who provided instructive feedback. R.L. acknowledges financial support from the Fund for Scientific Research – Flanders (FWO) under grant number ZKB5757-04-W01, and from the Department of Physics and Astronomy of the KU Leuven. L.D., E.D.B., and B.d.V. acknowledge financial support from the FWO. J.B. and P.R. acknowledge support from the Belgian Federal Science Policy Office via the PRODEX Program of ESA. PACS has been developed by a consortium of institutes led by MPE (Germany) and including UVIE (Austria); KUL, CSL, IMEC (Belgium); CEA, OAMP (France); MPIA (Germany); IFSI, OAP/AOT, OAA/CAISMI, LENS, SISSA (Italy); IAC (Spain). This development has been supported by the funding agencies BMVIT (Austria), ESA-PRODEX (Belgium), CEA/CNES (France), DLR (Germany), ASI (Italy), and CICT/MCT (Spain). For the computations we used the infrastructure of the VSC – Flemish Supercomputer Center, funded by the Hercules Foundation and the Flemish Government – department EWI.

References

Arenou, F., Grenon, M., & Gomez, A. 1992, A&A, 258, 104
Barlow, M. J., Nguyen-Q-Rieu, Truong-Bach, et al. 1996, A&A, 315, L241
Beck, H. K. B., Gail, H.-P., Henkel, R., & Sedlmayr, E. 1992, A&A, 265, 626
Bertie, J. E., Labbé, H. J., & Whalley, E. 1969, J. Chem. Phys., 50, 4501
Bohren, C. F., & Huffman, D. R. 1983, Absorption and scattering of light by small particles (New York: Wiley)
Bowers, P. F., & Johnston, K. J. 1990, ApJ, 354, 676
Bujarrabal, V., & Alcolea, J. 1991, A&A, 251, 536
Cherchneff, I. 2006, A&A, 456, 1001
Chiar, J. E., & Tielens, A. G. G. M. 2006, ApJ, 637, 774
Clegg, P. E., Ade, P. A. R., Armand, C., et al. 1996, A&A, 315, L38
De Beck, E., Decin, L., de Koter, A., et al. 2010, A&A, 523, A18
de Graauw, T., Haser, L. N., Beintema, D. A., et al. 1996, A&A, 315, L49
de Graauw, T., Helmich, F. P., Phillips, T. G., et al. 2010, A&A, 518, L6
de Vries, B. L., Min, M., Waters, L. B. F. M., Blommaert, J. A. D. L., & Kemper, F. 2010, A&A, 516, A86
Decin, L., & Eriksson, K. 2007, A&A, 472, 1041
Decin, L., Hony, S., de Koter, A., et al. 2006, A&A, 456, 549
Decin, L., Hony, S., de Koter, A., et al. 2007, A&A, 475, 233
Decin, L., De Beck, E., Brünken, S., et al. 2010a, A&A, 516, A69
Decin, L., Justtanont, K., De Beck, E., et al. 2010b, A&A, 521, L4
Delfosse, X., Kahane, C., & Forveille, T. 1997, A&A, 320, 249
Dijkstra, C., Dominik, C., Hoogzaad, S. N., de Koter, A., & Min, M. 2003, A&A, 401, 599
Dijkstra, C., Dominik, C., Bouwman, J., & de Koter, A. 2006, A&A, 449, 1101
Elitzur, M., Goldreich, P., & Scoville, N. 1976, ApJ, 205, 384
Engels, D., Schmid-Burgk, J., & Walmsley, C. M. 1986, A&A, 167, 129
Gilman, R. C. 1969, ApJ, 155, L185
Gray, M. D., Howe, D. A., & Lewis, B. M. 2005, MNRAS, 364, 783
Groenewegen, M. A. T., Waelkens, C., Barlow, M. J., et al. 2011, A&A, 526, A162
Gustafsson, B., Edvardsson, B., Eriksson, K., et al. 2008, A&A, 486, 951
Habing, H. J. 1968, Bull. Astron. Inst. Netherlands, 19, 421
Habing, H. J., & Olofsson, H. 2003, Asymptotic giant branch stars (New York, Berlin: Springer)
Henning, T., & Stognienko, R. 1996, A&A, 311, 291
Herman, J., & Habing, H. J. 1985, A&AS, 59, 523
Heske, A., Forveille, T., Omont, A., van der Veen, W. E. C. J., & Habing, H. J. 1990, A&A, 239, 173
Höfner, S. 2008, A&A, 491, L1
Jäger, C., Molster, F. J., Dorschner, J., et al. 1998, A&A, 339, 904
Justtanont, K., & Tielens, A. G. G. M. 1992, ApJ, 389, 400
Kama, M., Min, M., & Dominik, C. 2009, A&A, 506, 1199
Kemper, F., de Koter, A., Waters, L. B. F. M., Bouwman, J., & Tielens, A. G. G. M. 2002, A&A, 384, 585
Kemper, F., Stark, R., Justtanont, K., et al. 2003, A&A, 407, 609
Kessler, M. F., Steinz, J. A., Anderegg, M. E., et al. 1996, A&A, 315, L27
Knapp, G. R., & Morris, M. 1985, ApJ, 292, 640
Kwok, S. 1975, ApJ, 198, 583
Lamers, H. J. G. L. M., & Cassinelli, J. P. 1999, Introduction to Stellar Winds (Cambridge University Press)
Lepine, J. R. D., Ortiz, R., & Epchtein, N. 1995, A&A, 299, 453
Loup, C., Forveille, T., Omont, A., & Paul, J. F. 1993, A&AS, 99, 291
MacGregor, K. B., & Stencel, R. E. 1992, ApJ, 397, 644
Maercker, M., Schöier, F. L., Olofsson, H., Bergman, P., & Ramstedt, S. 2008, A&A, 479, 779
Maercker, M., Schöier, F. L., Olofsson, H., et al. 2009, A&A, 494, 243
Mamon, G. A., Glassgold, A. E., & Huggins, P. J. 1988, ApJ, 328, 797
Mathis, J. S., Rumpl, W., & Nordsieck, K. H. 1977, ApJ, 217, 425
Menten, K. M., & Melnick, G. J. 1989, ApJ, 341, L91
Menten, K. M., Philipp, S. D., Güsten, R., et al. 2006, A&A, 454, L107
Min, M., Hovenier, J. W., & de Koter, A. 2003, A&A, 404, 35
Min, M., Dullemond, C. P., Dominik, C., de Koter, A., & Hovenier, J. W. 2009, A&A, 497, 155
Netzer, N., & Knapp, G. R. 1987, ApJ, 323, 734
Neufeld, D. A., Chen, W., Melnick, G. J., et al. 1996, A&A, 315, L237
Norris, B. R. M., Tuthill, P. G., Ireland, M. J., et al. 2012, Nature, 484, 220

Olofsson, H. 2008, Phys. Scr. T, 133, 014028
Omont, A., Forveille, T., Moseley, S. H., et al. 1990, ApJ, 355, L27
Pilbratt, G. L., Riedinger, J. R., Passvogel, T., et al. 2010, A&A, 518, L1
Poglitsch, A., Waelkens, C., Geis, N., et al. 2010, A&A, 518, L2
Redfield, S., & Linsky, J. L. 2008, ApJ, 673, 283
Renzini, A. 1981, in Physical Processes in Red Giants, eds. I. Iben Jr., & A. Renzini, ASSL, 88, 431
Russell, H. N. 1934, ApJ, 79, 317
Servoin, J. L., & Piriou, B. 1973, Phys. Status Solidi B, 55, 677
Skinner, C. J., Justtanont, K., Tielens, A. G. G. M., et al. 1999, MNRAS, 302, 293
Sloan, G. C., Kraemer, K. E., Price, S. D., & Shipman, R. F. 2003, ApJS, 147, 379
Suh, K. 2004, ApJ, 615, 485
Suh, K., & Kim, H. 2002, A&A, 391, 665
Swinyard, B. M., Clegg, P. E., Ade, P. A. R., et al. 1996, A&A, 315, L43
Sylvester, R. J., Barlow, M. J., Nguyen-Q-Rieu, et al. 1997, MNRAS, 291, L42
Sylvester, R. J., Kemper, F., Barlow, M. J., et al. 1999, A&A, 352, 587
Tielens, A. G. G. M. 2005, The Physics and Chemistry of the Interstellar Medium (Cambridge University Press)
Tielens, A. G. G. M., & Allamandola, L. J. 1987, in Interstellar Processes, eds. D. J. Hollenbach, & H. A. Thronson Jr., ASSL, 134, 397
Truong-Bach, Morris, D., & Nguyen-Q-Rieu. 1991, A&A, 249, 435
Truong-Bach, Sylvester, R. J., Barlow, M. J., et al. 1999, A&A, 345, 925
van Langevelde, H. J., van der Heiden, R., & van Schooneveld, C. 1990, A&A, 239, 193
Warren, S. G. 1984, Appl. Opt., 23, 1206
Whitelock, P., Feast, M., & Catchpole, R. 1991, MNRAS, 248, 276
Whitelock, P., Menzies, J., Feast, M., et al. 1994, MNRAS, 267, 711
Whittet, D. C. B. 1992, Dust in the galactic environment (Institute of Physics Publishing)

Pages 18 to 19 are available in the electronic edition of the journal at http://www.aanda.org

Appendix A: Integrated line strengths

Table A.1 lists integrated line strengths of all detected ortho- and para-H_2O vapor emission lines and the 1612 MHz OH maser formation rotational cascade lines in the PACS spectrum shown in Figs. 10 and 11. Because the OH emission lines occur in doublets, the integrated line strengths for both components have been summed. We refer to Sylvester et al. (1997) for details on OH spectroscopy. Where confusion due to line blending occurs, we indicate this clearly, as well as list all H_2O transitions that may contribute to the emission line. As such we cannot distinguish the relative contribution of each transition in the blend. Blends that might be caused by the emission of other molecules not modeled in this study are not indicated.

Table A.1. Integrated line strength $F_{\rm int}$ (W/m^2) of detected ortho- and para-H_2O vapor emission lines and the 1612 MHz OH maser formation rotational cascade lines in the PACS spectrum shown in Figs. 10 and 11.

PACS band	Molecule	Vibrational state	Rotational transition	λ_0 μm	$F_{\rm int}$ (W/m^2)
B2A	o-H_2O	$v = 0$	$J_{K_a,K_c} = 4_{3,2}-3_{2,1}$	58.70	1.99e-16 (25.8%)
	o-H_2O	$v_3 = 1$	$J_{K_a,K_c} = 4_{3,1}-3_{2,2}$	58.89	6.64e-17 (45.2%)
	p-H_2O	$v = 0$	$J_{K_a,K_c} = 7_{2,6}-6_{1,5}$	59.99	* 1.51e-16 (38.6%)
	p-H_2O	$v = 0$	$J_{K_a,K_c} = 8_{2,6}-7_{3,5}$	60.16	^{b} 8.90e-17 (34.8%)
	o-H_2O	$v_2 = 1$	$J_{K_a,K_c} = 3_{3,0}-2_{2,1}$	60.49	^{b} 8.65e-17 (40.6%)
	o-H_2O	$v = 0$	$J_{K_a,K_c} = 6_{6,1}-6_{5,2}$	63.91	* 4.50e-16 (23.1%)
	o-H_2O	$v = 0$	$J_{K_a,K_c} = 6_{6,0}-6_{5,1}$	63.93	
	o-H_2O	$v_2 = 1$	$J_{K_a,K_c} = 8_{0,8}-7_{1,7}$	63.95	
	o-H_2O	$v = 0$	$J_{K_a,K_c} = 7_{6,1}-7_{5,2}$	63.96	
	o-H_2O	$v = 0$	$J_{K_a,K_c} = 6_{2,5}-5_{1,4}$	65.17	^{*,b} 1.31e-16 (35.2%)
	o-H_2O	$v = 0$	$J_{K_a,K_c} = 3_{3,0}-2_{2,1}$	66.44	^{b} 1.28e-16 (29.0%)
	p-H_2O	$v = 0$	$J_{K_a,K_c} = 3_{3,1}-2_{2,0}$	67.09	* 2.59e-16 (23.1%)
	p-H_2O	$v_2 = 1$	$J_{K_a,K_c} = 5_{2,4}-4_{1,3}$	67.26	* 1.52e-16 (25.2%)
	p-H_2O	$v = 0$	$J_{K_a,K_c} = 3_{3,0}-3_{0,3}$	67.27	
	o-H_2O	$v_2 = 1$	$J_{K_a,K_c} = 3_{2,1}-2_{1,2}$	70.29	7.59e-17 (27.8%)
	o-H_2O	$v = 0$	$J_{K_a,K_c} = 8_{2,7}-8_{1,8}$	70.70	1.31e-16 (22.4%)
	p-H_2O	$v = 0$	$J_{K_a,K_c} = 5_{2,4}-4_{1,3}$	71.07	^{b} 1.92e-16 (22.6%)
	p-H_2O	$v = 0$	$J_{K_a,K_c} = 7_{1,7}-6_{0,6}$	71.54	1.11e-16 (29.2%)
	o-H_2O	$v = 0$	$J_{K_a,K_c} = 7_{0,7}-6_{1,6}$	71.95	1.28e-16 (26.3%)
B2B	o-H_2O	$v_2 = 1$	$J_{K_a,K_c} = 3_{2,1}-2_{1,2}$	70.29	* 1.14e-16 (34.4%)
	o-H_2O	$v = 0$	$J_{K_a,K_c} = 8_{2,7}-8_{1,8}$	70.70	1.27e-16 (29.1%)
	p-H_2O	$v = 0$	$J_{K_a,K_c} = 5_{2,4}-4_{1,3}$	71.07	^{b} 1.88e-16 (22.8%)
	p-H_2O	$v = 0$	$J_{K_a,K_c} = 7_{1,7}-6_{0,6}$	71.54	9.54e-17 (31.8%)
	o-H_2O	$v = 0$	$J_{K_a,K_c} = 7_{0,7}-6_{1,6}$	71.95	1.47e-16 (25.8%)
	p-H_2O	$v = 0$	$J_{K_a,K_c} = 9_{3,7}-9_{2,8}$	73.61	9.09e-17 (26.0%)
	o-H_2O	$v = 0$	$J_{K_a,K_c} = 7_{2,5}-6_{3,4}$	74.95	1.26e-16 (22.7%)
	o-H_2O	$v = 0$	$J_{K_a,K_c} = 3_{2,1}-2_{1,2}$	75.38	^{b} 1.05e-16 (23.7%)
	o-H_2O	$v = 0$	$J_{K_a,K_c} = 8_{5,4}-8_{4,5}$	75.50	5.40e-17 (31.8%)
	p-H_2O	$v = 0$	$J_{K_a,K_c} = 5_{5,1}-5_{4,2}$	75.78	* 3.11e-16 (21.1%)
	p-H_2O	$v = 0$	$J_{K_a,K_c} = 7_{5,3}-7_{4,4}$	75.81	
	p-H_2O	$v = 0$	$J_{K_a,K_c} = 6_{5,2}-6_{4,3}$	75.83	
	o-H_2O	$v = 0$	$J_{K_a,K_c} = 5_{5,0}-5_{4,1}$	75.91	* 1.09e-16 (26.8%)
	p-H_2O	$v = 0$	$J_{K_a,K_c} = 6_{5,1}-6_{4,2}$	76.42	1.08e-16 (25.4%)
	o-H_2O	$v = 0$	$J_{K_a,K_c} = 7_{5,2}-7_{4,3}$	77.76	^{b} 7.39e-17 (25.6%)
	o-H_2O	$v = 0$	$J_{K_a,K_c} = 4_{2,3}-3_{1,2}$	78.74	1.43e-16 (22.8%)
	p-H_2O	$v = 0$	$J_{K_a,K_c} = 6_{1,5}-5_{2,4}$	78.93	* 8.61e-17 (26.6%)
	p-H_2O	$v_2 = 1$	$J_{K_a,K_c} = 6_{4,3}-6_{3,4}$	78.95	
	OH	$v = 0$	$^2\Pi_{1/2}J = 1/2-{}^2\Pi_{3/2}J = 3/2$	79.12-79.18	^{a} 3.09e-16 (35.9%)
	o-H_2O	$v = 0$	$J_{K_a,K_c} = 8_{3,6}-8_{2,7}$	82.98	9.18e-17 (25.7%)
	p-H_2O	$v_2 = 1$	$J_{K_a,K_c} = 3_{2,2}-2_{1,1}$	83.24	5.26e-17 (39.8%)
	p-H_2O	$v = 0$	$J_{K_a,K_c} = 6_{0,6}-5_{1,5}$	83.28	8.80e-17 (28.1%)
	o-H_2O	$v = 0$	$J_{K_a,K_c} = 7_{1,6}-7_{0,7}$	84.77	* 1.56e-16 (22.9%)
	o-H_2O	$v = 0$	$J_{K_a,K_c} = 8_{4,5}-8_{3,6}$	85.77	* 6.92e-17 (25.5%)
	o-H_2O	$v_2 = 1$	$J_{K_a,K_c} = 6_{4,2}-6_{3,3}$	85.78	
	p-H_2O	$v = 0$	$J_{K_a,K_c} = 3_{2,2}-2_{1,1}$	89.99	* 1.49e-16 (22.9%)
	p-H_2O	$v = 0$	$J_{K_a,K_c} = 7_{4,4}-7_{3,5}$	90.05	8.09e-17 (24.0%)
	o-H_2O	$v = 0$	$J_{K_a,K_c} = 6_{4,3}-6_{3,4}$	92.81	^{b} 1.20e-16 (21.8%)

Notes. The rest wavelength λ_0 (μm) of the transition is indicated. The percentages between brackets indicate the uncertainty on $F_{\rm int}$, which includes both the fitting uncertainty and the PACS absolute flux calibration uncertainty of 20%. $^{(\star)}$ Line strengths flagged for potential line blends (see Sect. 2.2.1). Transitions that might cause the line blend are mentioned immediately below the flagged transition. $^{(a)}$ Transition detected in an emission doublet. The given value is the sum of the line strengths of both emission lines in the doublet. $^{(b)}$ The selection of H_2O vapor emission lines based on which we have derived the H_2O vapor abundance (see Sect. 4.2.3).

Table A.1. continued.

PACS band	Molecule	Vibrational state	Rotational transition	λ_0 μm	$F_{\rm int}$ (W/m^2)
	p-H_2O	$\nu = 0$	$J_{K_a,K_c} = 7_{3,5}-7_{2,6}$	93.38	9.90e-17 (22.4%)
	o-H_2O	$\nu = 0$	$J_{K_a,K_c} = 6_{5,2}-7_{2,5}$	94.17	⋆ 1.07e-16 (23.7%)
	o-H_2O	$\nu = 0$	$J_{K_a,K_c} = 5_{4,2}-5_{3,3}$	94.21	
	o-H_2O	$\nu_3 = 1$	$J_{K_a,K_c} = 7_{4,4}-7_{3,5}$	94.61	⋆ 1.10e-16 (23.4%)
	o-H_2O	$\nu = 0$	$J_{K_a,K_c} = 6_{2,5}-6_{1,6}$	94.64	
	o-H_2O	$\nu = 0$	$J_{K_a,K_c} = 4_{4,1}-4_{3,2}$	94.71	1.40e-16 (22.5%)
	p-H_2O	$\nu_2 = 1$	$J_{K_a,K_c} = 5_{1,5}-4_{0,4}$	94.90	4.91e-17 (32.5%)
	o-H_2O	$\nu = 0$	$J_{K_a,K_c} = 9_{4,5}-8_{5,4}$	95.18	2.26e-17 (40.0%)
	p-H_2O	$\nu = 0$	$J_{K_a,K_c} = 5_{1,5}-4_{0,4}$	95.63	8.59e-17 (28.8%)
	p-H_2O	$\nu = 0$	$J_{K_a,K_c} = 4_{4,0}-4_{3,1}$	95.88	[b] 9.46e-17 (26.3%)
	o-H_2O	$\nu = 0$	$J_{K_a,K_c} = 5_{4,1}-5_{3,2}$	98.49	⋆ 6.85e-17 (51.4%)
	OH	$\nu = 0$	$^2\Pi_{1/2}J = 5/2-^2\Pi_{1/2}J = 3/2$	98.72-98.74	⋆,[a] 1.54e-16 (29.6%)
	p-H_2O	$\nu_2 = 1$	$J_{K_a,K_c} = 8_{3,5}-7_{4,4}$	98.73	
R1A	p-H_2O	$\nu = 0$	$J_{K_a,K_c} = 6_{4,2}-6_{3,3}$	103.92	⋆ 1.70e-16 (23.4%)
	p-H_2O	$\nu = 0$	$J_{K_a,K_c} = 6_{1,5}-6_{0,6}$	103.94	
	o-H_2O	$\nu = 0$	$J_{K_a,K_c} = 6_{3,4}-6_{2,5}$	104.09	1.27e-16 (26.4%)
	o-H_2O	$\nu_3 = 1$	$J_{K_a,K_c} = 2_{2,0}-1_{1,1}$	104.81	4.15e-17 (39.1%)
	o-H_2O	$\nu = 0$	$J_{K_a,K_c} = 2_{2,1}-1_{1,0}$	108.07	[b] 1.25e-16 (21.4%)
	p-H_2O	$\nu = 0$	$J_{K_a,K_c} = 5_{2,4}-5_{1,5}$	111.63	9.51e-17 (24.1%)
	o-H_2O	$\nu = 0$	$J_{K_a,K_c} = 7_{4,3}-7_{3,4}$	112.51	3.53e-17 (33.9%)
	o-H_2O	$\nu_2 = 1$	$J_{K_a,K_c} = 6_{4,3}-7_{1,6}$	112.80	⋆ 3.20e-17 (39.4%)
	o-H_2O	$\nu = 0$	$J_{K_a,K_c} = 4_{4,1}-5_{1,4}$	112.80	
	o-H_2O	$\nu_3 = 1$	$J_{K_a,K_c} = 5_{2,4}-5_{1,5}$	112.89	
	o-H_2O	$\nu = 0$	$J_{K_a,K_c} = 4_{1,4}-3_{0,3}$	113.54	9.06e-17 (23.7%)
	p-H_2O	$\nu = 0$	$J_{K_a,K_c} = 5_{3,3}-5_{2,4}$	113.95	1.24e-16 (21.9%)
	o-H_2O	$\nu = 0$	$J_{K_a,K_c} = 4_{3,2}-4_{2,3}$	121.72	[b] 9.60e-17 (21.2%)
	p-H_2O	$\nu = 0$	$J_{K_a,K_c} = 8_{4,4}-8_{3,5}$	122.52	2.63e-17 (34.0%)
	o-H_2O	$\nu = 0$	$J_{K_a,K_c} = 9_{3,6}-9_{2,7}$	123.46	3.11e-17 (30.1%)
	o-H_2O	$\nu_2 = 1$	$J_{K_a,K_c} = 5_{1,4}-5_{0,5}$	124.85	⋆ 5.90e-17 (24.5%)
	p-H_2O	$\nu = 0$	$J_{K_a,K_c} = 4_{0,4}-3_{1,3}$	125.35	7.52e-17 (22.4%)
	p-H_2O	$\nu = 0$	$J_{K_a,K_c} = 3_{3,1}-3_{2,2}$	126.71	[b] 8.53e-17 (21.6%)
	o-H_2O	$\nu = 0$	$J_{K_a,K_c} = 7_{2,5}-7_{1,6}$	127.88	⋆ 6.84e-17 (26.4%)
	o-H_2O	$\nu = 0$	$J_{K_a,K_c} = 9_{4,5}-9_{3,6}$	129.34	4.27e-17 (24.0%)
	o-H_2O	$\nu = 0$	$J_{K_a,K_c} = 4_{2,3}-4_{1,4}$	132.41	8.39e-17 (21.3%)
	o-H_2O	$\nu = 0$	$J_{K_a,K_c} = 5_{1,4}-5_{0,5}$	134.94	[b] 7.45e-17 (22.2%)
	o-H_2O	$\nu = 0$	$J_{K_a,K_c} = 3_{3,0}-3_{2,1}$	136.50	8.01e-17 (21.7%)
	p-H_2O	$\nu = 0$	$J_{K_a,K_c} = 3_{1,3}-2_{0,2}$	138.53	⋆ 7.59e-17 (21.7%)
	p-H_2O	$\nu = 0$	$J_{K_a,K_c} = 8_{4,4}-7_{5,3}$	138.64	
	p-H_2O	$\nu_2 = 1$	$J_{K_a,K_c} = 6_{3,3}-6_{2,4}$	140.06	⋆ 2.99e-17 (31.7%)
	p-H_2O	$\nu = 0$	$J_{K_a,K_c} = 4_{1,3}-3_{2,2}$	144.52	[b] 4.63e-17 (23.5%)
R1B	p-H_2O	$\nu = 0$	$J_{K_a,K_c} = 4_{1,3}-3_{2,2}$	144.52	[b] 4.80e-17 (23.7%)
	p-H_2O	$\nu = 0$	$J_{K_a,K_c} = 4_{3,1}-4_{2,2}$	146.92	6.72e-17 (22.0%)
	o-H_2O	$\nu_3 = 1$	$J_{K_a,K_c} = 8_{3,5}-8_{2,6}$	148.64	⋆ 5.12e-17 (25.3%)
	o-H_2O	$\nu = 0$	$J_{K_a,K_c} = 8_{3,5}-8_{2,6}$	148.71	
	o-H_2O	$\nu = 0$	$J_{K_a,K_c} = 5_{4,2}-6_{1,5}$	148.79	
	o-H_2O	$\nu_2 = 1$	$J_{K_a,K_c} = 2_{2,1}-2_{1,2}$	153.27	1.51e-17 (33.8%)
	p-H_2O	$\nu_2 = 1$	$J_{K_a,K_c} = 6_{2,4}-6_{1,5}$	154.02	1.01e-17 (45.7%)
	p-H_2O	$\nu = 0$	$J_{K_a,K_c} = 3_{2,2}-3_{1,3}$	156.19	⋆ 1.28e-16 (20.7%)
	p-H_2O	$\nu = 0$	$J_{K_a,K_c} = 5_{2,3}-4_{3,2}$	156.27	
	o-H_2O	$\nu = 0$	$J_{K_a,K_c} = 5_{3,2}-5_{2,3}$	160.51	[b] 4.60e-17 (23.6%)
	OH	$\nu = 0$	$^2\Pi_{1/2}J = 3/2-^2\Pi_{1/2}J = 1/2$	163.12-163.4	[a] 1.47e-16 (30.5%)
	o-H_2O	$\nu = 0$	$J_{K_a,K_c} = 7_{3,4}-7_{2,5}$	166.81	⋆ 3.77e-17 (31.7%)
	o-H_2O	$\nu_3 = 1$	$J_{K_a,K_c} = 6_{2,4}-6_{1,5}$	166.83	
	p-H_2O	$\nu = 0$	$J_{K_a,K_c} = 6_{2,4}-6_{1,5}$	167.03	4.11e-17 (27.9%)
	p-H_2O	$\nu = 0$	$J_{K_a,K_c} = 6_{3,3}-6_{2,4}$	170.14	⋆ 4.50e-17 (35.1%)
	p-H_2O	$\nu = 0$	$J_{K_a,K_c} = 5_{3,3}-6_{0,6}$	174.61	⋆ 8.25e-17 (21.9%)
	p-H_2O	$\nu = 0$	$J_{K_a,K_c} = 3_{0,3}-2_{1,2}$	174.63	
	p-H_2O	$\nu_3 = 1$	$J_{K_a,K_c} = 3_{0,3}-2_{1,2}$	174.66	
	o-H_2O	$\nu = 0$	$J_{K_a,K_c} = 4_{3,2}-5_{0,5}$	174.92	1.49e-17 (43.1%)
	o-H_2O	$\nu = 0$	$J_{K_a,K_c} = 2_{1,2}-1_{0,1}$	179.53	[b] 4.93e-17 (24.1%)
	o-H_2O	$\nu = 0$	$J_{K_a,K_c} = 2_{2,1}-2_{1,2}$	180.49	[b] 5.87e-17 (26.7%)